運輸省港湾技術研究所 (25th Anniversary Issue)

港湾技術研究所報告

REPORT OF THE PORT AND HARBOUR RESEARCH INSTITUTE

MINISTRY OF TRANSPORT

VOL. 26 NO. 5 DEC. 1987

NAGASE, YOKOSUKA, JAPAN

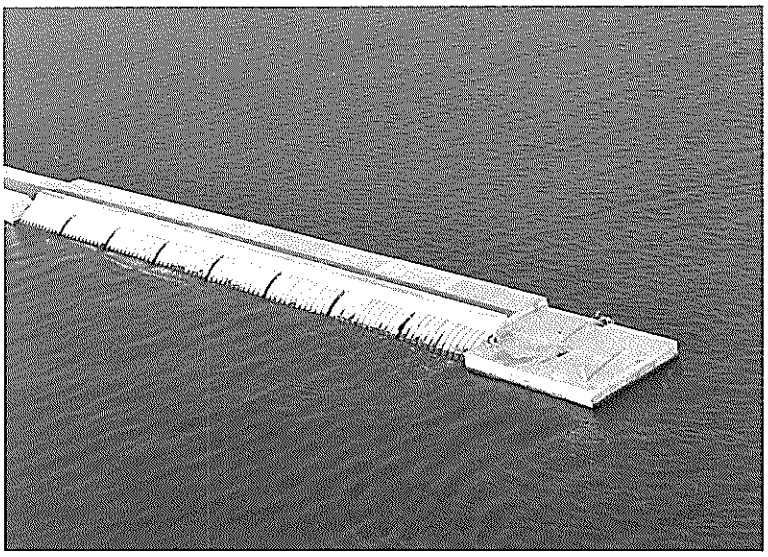

Curved Slit Caisson Breakwater

View of curved slit caisson breakwater completed in the construction at the port of Funakawa. (Courtesy of Akita Port Construction Office, the First District Port Construction Bureau, Ministry of Transport)

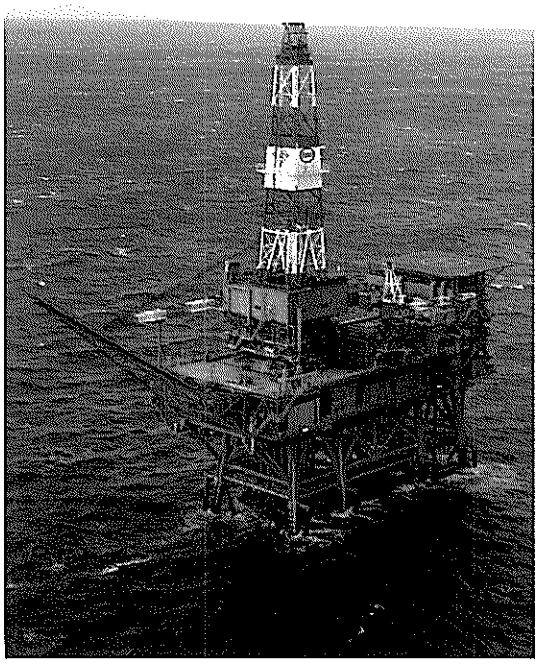

Facilities for Ocean Directional Wave Measurement

Four step type wave gauges and a two-axis directional current meter with a pressure sensor are installed on the legs of an offshore oil rig. They are operated simultaneously for detailed directional wave analysis.

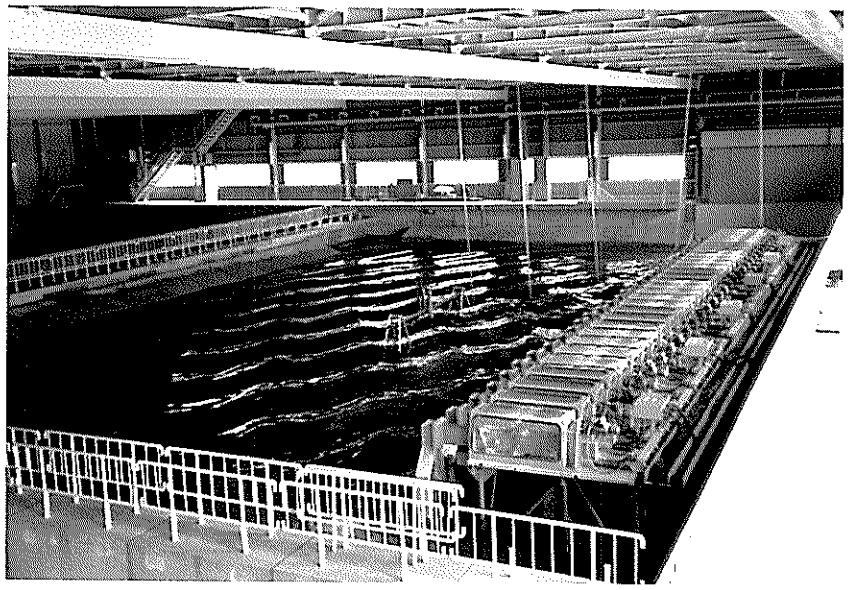

Serpent-type Wave Generator

The photograph shows the serpent-type wave generator in the short-crested wave basin and the superimposition state of two different oblique waves generated by the generator.

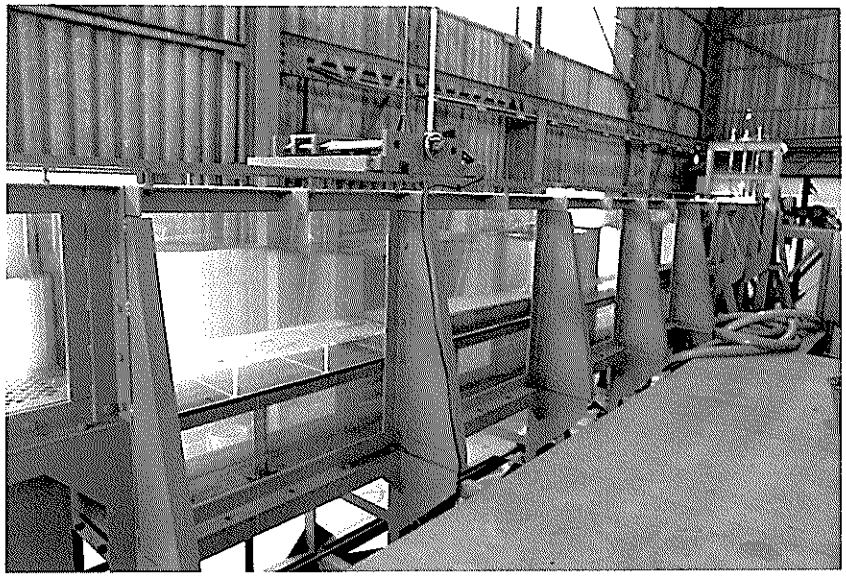

Wave-soil Tank

The experiments concerning the wave-soil interactions are conducted in this tank. The soil tank and the test section are located at the center of the tank. A movable floor is provided at the bottom of the test section and the level of the interface of mud layer and water can easily be adjusted to the level of the flume bottom.

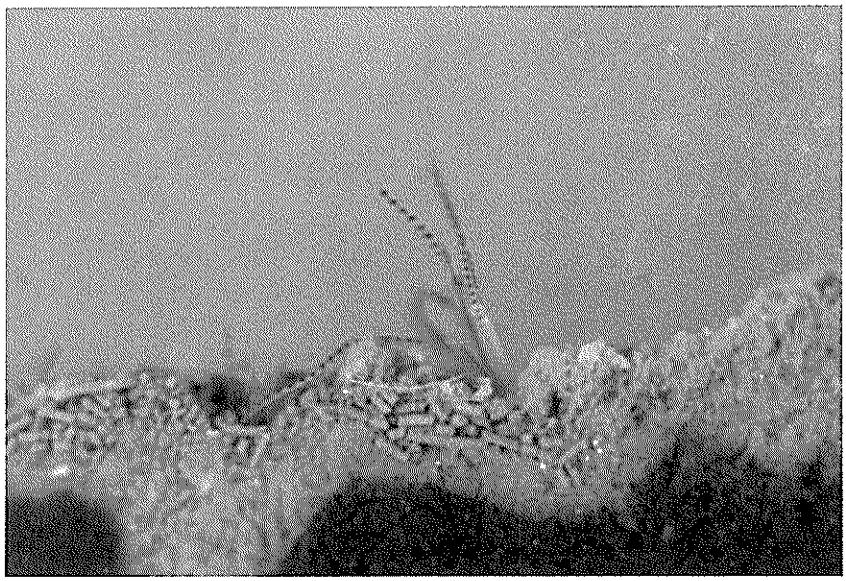

Pararionospio Pinnata

The biomass of benthos is one of the most sensitive indices to know the effect of sea-bed sediment treatments on the marine environmental improvement. The picure shows a kind of benthos, *pararionospio pinnata,* which preferentially exists in the polluted sea-bed.

Breakwater Damaged by Storm

This photograph shows a breakwater damage by a storm.
The breakwater is of the composite type with concrete caisson on a rubble mound. Two caissons were severly damaged due to the instability of a rubble mound.

Nondestructive Evaluation of Pavement

Nondestructive methods for evaluating the load carrying capacity of airport concrete pavements have been developed by using Falling Weight Deflectometer(FWD).

Seismic Damage to Gravity Quaywall

The 1983 Nipponkai-Chubu earthquake(Magnitude : 7.7)caused serious damage to port facilities in northern part of Japan. This photo shows the damage to gravity quaywall. The concrete cellular block walls were collapsed and completely submerged.

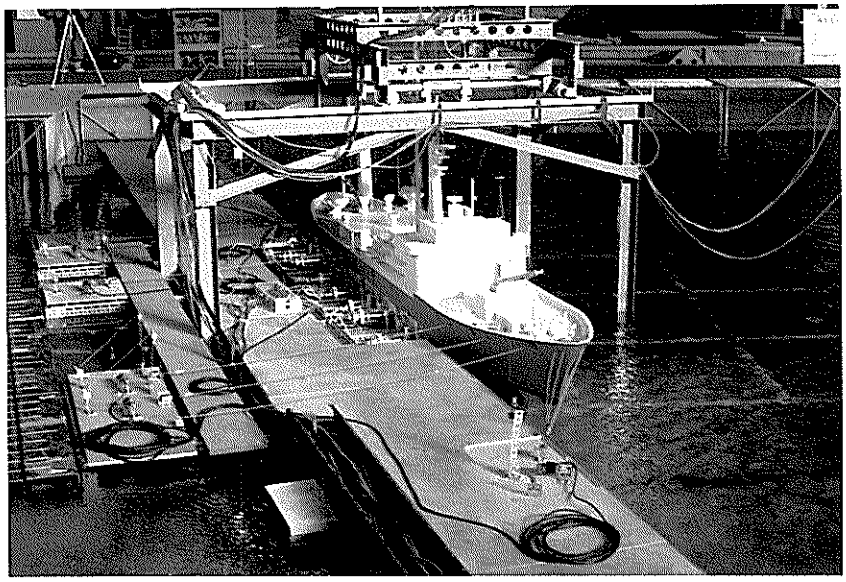

Model Experiment of Mooring Ship

Model ship is moored at a quay wall with fenders and mooring ropes subjected to gusty wind and/or irregular waves.

Vessel Congestion in Japan

As Japan is surrounded by the sea, there are many crowded water areas with various sizes and types of vessels. Arround there, many construction works were planned such as ports and harbours, off-shore airports, huge bridges and so on, so that many marine traffic observations and marine traffic simulations have been carried out.

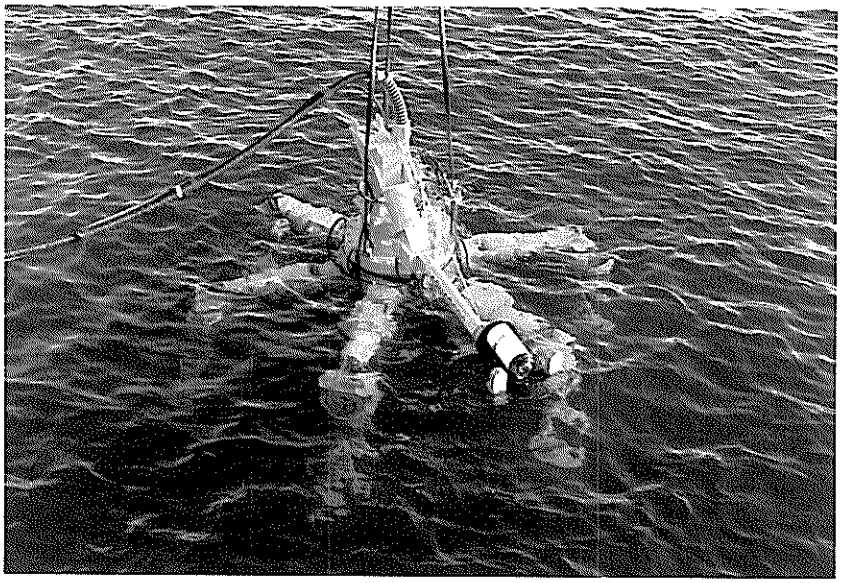

Underwater Inspection Robot

This is the six-legged articulated underwater inspection robot named "AQUAROBOT". The robot controlled by a computer can walk on uneven sea bed without making water muddy.

Foreword

The Port and Harbour Research Institute is a national laboratory under the Ministry of Transport, Japan. It is responsible for solving various engineering problems related to port and harbour projects so that governmental agencies in charge of port development can execute the projects smoothly and rationally. Its research activities also cover the studies on civil engineering facilities of air ports.

Last April we have celebrated the 25th anniversary of our institute because the present organization was established in 1962, though systematic research works on ports and harbours under the Ministry of Transport began in 1946. As an event for the celebration, we decided to publish a special edition of the Report of the Port and Harbour Research Institute, which contains full English papers only. These papers are so selected to introduce the versatility of our activities and engineering practices in Japan to overseas engineers and scientists. It is also intended to remedy to a certain extent the information gap between overseas colleagues and us.

The reader will find that our research fields cover physical oceanography, coastal and ocean engineering, geotechnical engineering, earthquake engineering, materials engineering, dredging technology and mechanical engineering, planning and systems analysis, and structural analysis. Such an expansion of the scope of research fields has been inevitable, because we are trying to cover every aspect of technical problems of ports and harbours as an integrated body.

The present volume contains eleven papers representing six research divisions of the institute. The materials introduced in these papers are not necessarily original in strict sense, as some parts have been published in Japanese in the Reports or the Technical Notes of the Port and Harbour Research Institute. Nevertheless they are all original papers in English and are given the full format accordingly. We expect that they will be referred to as usual where they deserve so.

It is my sincere wish that this special edition of the Report of the Port and Harbour Research Institute will bring overseas engineers and scientists more acquainted with our research activities and enhance the mutual cooperation for technology development related to ports and harbours.

December 1987
Yoshimi Goda
Director General

港湾技術研究所報告 (REPORT OF P. H. R. I.)
第26巻 第5号 (Vol. 26, No. 5) 1987年12月 (Dce. 1987)

目　　次 (CONTENTS)

REPORT OF THE PORT AND
HARBOUR RESEARCH INSTITUTE
Vol. 26, No. 5 (Dec. 1987)

4. Interactions between Surface Waves and a Multi-Layered Mud Bed

Hiroichi TSURUYA*
Susumu NAKANO**
Jun TAKAHAMA***

Synopsis

A multi-layered viscous fluid model is presented to investigate the wave field and mass transport velocity of mud layers under the action of surface waves. Essentially, the model treats the fluid system as Newtonian and the equivalent viscosity is proposed to introduce the nature of a Bingham fluid into mud layers.

In the model, viscosities of mud layers are estimated by the iteration procedures and it is required to give only the total depth of mud layers which are in motion. The validity of the theory is checked by comparison with the experimental results.

From the rotary visco-meter tests, it is confirmed that mud exhibits the properties of a Bingham fluid when the shear rate is less than $1\ s^{-1}$.

Experiments were conducted in a 11 m long, 0.4 m wide and 0.5 m high soil-wave tank. Kaolinite clay was used for the bed material. The ratio of water content of mud varied from 165% to 410%. Naturally settled kaolinite and natural mud which was sampled at Ariake Bay were also used as bed materials. In the experiment, the mud depth was set at 10 cm and 20 cm. Sinusoidal regular waves were generated by a plunger-type wave maker. The wave period was varied from 0.7s to 1.4s for wave heights from 1.3 cm to 7.9 cm.

Surface waves were measured at five stations along the center line of the tank. The movement of the mud surface was measured by using an ultra-sonic depth sounder.

The damping factors and wave lengths of surface waves, pore pressures and mud particle trajectories were obtained from the experiments. These results almost coincide with the theoretical values, especially when the mud depth is shallow.

The theoretical mass transport velocities are obtained for the multi-layered viscous fluid model. The mass transport velocity in horizontal direction decreases as the ratio of water content increases. It is confirmed that the vertical mass transport velocity also exists and has the maximum value at the mud surface. The existence of vertical mass transport suggests that the rate of water content gradually increases with time.

When the rate of water content of mud layer is uniform, the damping factor of the surface waves decreases as the wave height increases, because the equivalent viscosity decreases.

* Chief of Hydrodynamics Laboratory, Marine Hydrodynamics Division
** Formerly, Member of Hydrodynamics Laboratory, Marine Hydrodynamics Division (Faculty of Engineering, Tokushima University)
*** Member of Hydrodynamics Laboratory, Marine Hydrodynamics Division

港湾技術研究所報告
第26巻 第5号 (1987.12)

4. 波と多層底泥の相互干渉に関する研究

鶴谷広一*・中野 晋**・鷹濱 潤***

要 旨

波と底泥の相互干渉について粘性流体に対する多層モデルを用いて検討した。一般に底泥は非ニュートン流体であるため，波動場で底泥の粘度を推定することは困難であるが，このモデルでは相当粘度の概念を導入して，波動場に応じた平均的な粘度分布を推定することが可能である。また，このモデルでは，波による底泥の質量輸送速度を計算することが可能になった。一般に，水平方向の質量輸送速度は含水比が大きくなるほど小さくなり，また常に鉛直方向の質量輸送速度も存在することがわかった。最後に，波と底泥の相互干渉についての実験を行い，波高減衰率，波長，底泥波，底泥内圧力変動，底泥粒子の運動等の実験結果を計算結果と比較し，モデルの適用性および限界について検討した。底泥としては，均質で扱いやすく，物理特性の良くわかっているカオリナイトを主として用いた。これを所定の含水比によく混合して水路床に敷き詰めた場合と，高さ4mの沈降塔にカオリナイトと水の混合水を入れて自然沈降させて水路内に底泥を形成させた場合について実験を行った。さらに，熊本で採取された現地泥についても実験を行っている。

実験結果を理論と比較すると，底泥厚が薄いケースの10cmの場合にはおおむね一致することが確認された。

* 海洋水理部 水理研究室長
** 前海洋水理部 水理研究室（現徳島大学工学部）
*** 海洋水理部 水理研究室

Contents

1. Introduction

A new port is under construction in Ariake bay off the coast of Kumamoto city. As the tidal range here is relatively large (4.5 m), and because three rivers flow into this area, cohesive sediment accumulates and forms a mud bed with a high water content. Such a bed can easily be deformed by small stresses and suspended sediment is carried out by waves and currents.

The movement of cohesive sediment causes problems such as silting in harbor entrance channels, docks and anchorages. Surface waves are one of the principal external forces which govern the siltation. Interaction between surface waves and the mud bed leads to the mass transport within the mud layer and the damping of the surface wave amplitudes.

Many types of investigations have been conducted for the interaction between surface waves and a mud bed. *Gade*[1] and *Dalrymple* and *Liu*[2] have treated the fluid system as a Newtonian. *Hsiao* and *Shemdin*[3] and *Macpherson*[4] have discussed the Voigt model in the sea-bed material. This model incorporates the viscosity and elasticity of the bed. However, it is not confirmed that the bed can be reasonably treated as a Voigt model. Moreover, it is difficult to evaluate the shear modulus of elasticity and the viscosity of the bed.

Yamamoto et al.[5),6),7] have developed theoretical models for wave-soil interactions which include the poro-elastic model, the Coulomb-damped elastic model and the Coulomb-damped poro-elastic model. It has been shown that the wave damping due to Coulomb friction in the clay bed is by far the largest damping mechanism when compared to other damping mechanism. These models are applicable for many types of bed materials from sand to clay. However, it is difficult to evaluate the shear modulus of the bed material.

Recent investigations of the rheological properties of cohesive sediment suspensions have shown that mud exhibits the properties of a non-Newtonian Fluid (*Otsubo*[8], *Tsuruya et al.*[9], *Faas*[10]). The authors[9] have shown that a mud bed can be characterized as a Bingham fluid within the range of shear stress under the action of surface waves.

From the standpoint of the views stated above, the present paper describes the theoretical and experimental investigations concerning the interactive effects between surface waves and a mud bed. A multi-layered viscous fluid model is proposed to analyze the interactions between surface waves and a mud bed. An equivalent viscosity which take the nature of Bingham fluid into consideration is utilized in the model.

2. Theoretical Considerations

2.1 Rheological Equations

Generally, the mud layer resembles like non-Newtonian Fluids. In order to investigate the motion of the mud layer, suitable equations of motion for the fluid must be adopted. In Fig. 1, the types of the fluid and rheological behaviors are shown on diagrams for the rate of deformation against the shear stress and viscosity. For Newtonian fluids, the shear stress is proportional to the rate of deformation,

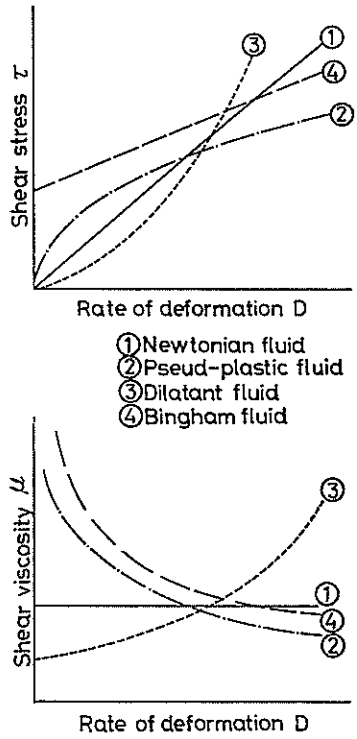

Fig. 1 Flow and Viscosity Curves for Different Kinds of Fluid

and the viscosity is constant. The solid lines ① represent the relations of Newtonian fluids. Another curves are for non-Newtonian fluids. Fluids having the nature of curves ② are termed pseudo-plastic and ③ dilatants. Bingham fluids (curves ④) have a yield stress below which they behave like a solid and above which they have fluidlike behavior.

Rheological equations which combine the stress and the rate of deformation (deformation-rate) are explained below[11].

For Newtonian fluids the rheological equation can be represented as

$$\sigma^i{}_j = -p\delta^i{}_j + 2\mu_N e^i{}_j, \tag{1}$$

where i and j take the value 1, 2, and 3 which correspond to x, y, and z axis, respectively, $\sigma^i{}_j$ the stress acting on a $i-j$ plane (when $i=j$, $\sigma^i{}_j$ corresponds to a normal stress acting on a i-plane, and when $i \neq j$, it corresponds to the shear stress acting on a $i-j$ plane), μ_N the dynamic viscosity for Newtonian fluids, $e^i{}_j$ the deformation-rate tensor.

For power law fluids, the relationship between the shear stress τ and the deformation-rate D can be expressed as

$$\tau = KD^n, \tag{2}$$

where K is the pseudo-plastic viscosity and n the constant. When $n<1$ the fluid is pseudo-plastic, $n=1$ ($K=\mu_N$) Newtonian and $n>1$ dilatants. The rheological equation for these fluids is

$$\sigma^i{}_j=-p\delta^i{}_j+2K[4|II_e|]^{(n-1)/2}e^i{}_j, \tag{3}$$

where $|II_e|$ is the objective of the deformation-rate tensor and expressed as

$$|II_e|=\frac{1}{2}\{(e^1{}_1)^2+(e^2{}_2)^2+(e^3{}_3)^2\}+\{(e^2{}_3)^2+(e^3{}_1)^2+(e^1{}_2)^2\}. \tag{4}$$

For Bingham fluids the relationship between τ and D can be expressed as

$$\tau=\tau_y+\mu_B D, \tag{5}$$

where τ_y is the yield stress and μ_B the plastic viscosity. Rheological equations for the fluid can be expressed as

$$\left.\begin{aligned}&\sigma^i{}_j=-p\delta^i{}_j+2\left(\mu_B+\frac{\tau_y}{\sqrt{4|II_e|}}\right)e^i{}_j, && \left(\frac{1}{2}p^i{}_jp^j{}_i>\tau_y{}^2\right)\\ &e^i{}_j=0, && \left(\frac{1}{2}p^i{}_jp^j{}_i\leqq\tau_y{}^2\right),\end{aligned}\right\} \tag{6}$$

where $p^i{}_j$ is the deviatoric stress tensor. Equation (6) shows that for shear stresses below the yield value, deformation of fluids does not occur. If we consider the two dimensional case of x and z axis, $e^i{}_j$ can be written as

$$e^1{}_1=e_{xx}=\frac{\partial u}{\partial x},\quad e^2{}_2=e_{zz}=\frac{\partial w}{\partial z},\quad e^1{}_2=e^2{}_1=e_{xz}=e_{zx}=\left(\frac{\partial u}{\partial z}+\frac{\partial w}{\partial x}\right).$$

So far we have described the rheological equations for the typical viscous fluids. The actual mud, however, usually behaves in a more complicated manner. Moreover, because of the strong nonlinearity of these equations, analytical solutions cannot be easily obtained and even numerical solutions cannot necessarily be obtained.

In the present study, therefore, equations of motion for Newtonian fluids are adopted and only in the estimation of the viscosity is the nature of non-Newtonian fluids considered.

We notice the second term in the right hand side of rheological equations (1), (3), and (6). All the shear stress tensors of three types of fluids can be expressed as

$$\alpha e^i{}_j,$$

where $\alpha=2\mu_N$ for Newtonian fluids, $\alpha=2K(4|II_e|)^{(n-1)/2}$ for power law fluids, and $2(\mu_B+\tau_y/\sqrt{4|II_e|})$ for Bingham fluids in the case of $(1/2)p^i{}_jp^j{}_i>\tau_y{}^2$. The coefficient α can be considered as the viscosity when fluids are deformed by stress. For Newtonian fluids α is constant but for non-Newtonian fluids α is a function of the objective $|II_e|$ and must have a value which depends on the motion of the fluids. As described above, it is very difficult to estimate the velocity field directly from the rheological equations. As the first approximation, therefore, we estimate the velocity field for Newtonian fluids and calculate the objective $|II_e|$ and the viscosity for the non-Newtonian fluids from it. Again, the velocity field is calculated by using the newly estimated viscosity. These procedures are repeated until the solutions converge. This method can estimate the viscosity corresponding to the flow field and allows us to investigate the approximate motion of non-Newtonian fluid.

2.2 Multi-Layered Viscous Fluid Model

In this model, it is assumed that the equations of motion for Newtonian fluid can be applied to a mud layer. Theoretical investigations of interactive effects between surface waves and a mud bottom have been conducted by *Dalrymple and Liu*[2] who treated the fluid system as a two-layered Newtonian. We expand it to a multi-layered fluid model taking into account the nature of a Bingham fluid.

The assumptions used in the model are as follows:

a. Waves are expressed as sinusoidal.
b. Motions are limited to the direction of wave propagation and the vertical direction, and the motion to the direction perpendicular to the wave propagation is negligibly small.
c. Lengths of the water area and the mud layer to the direction of wave propagation are infinite.
d. The mud layer is horizontal, and the water depth and the mud layer thickness constant.
e. The amplitudes of waves are small compared with the water depth.
f. Convective accelerations in the Navier-Stokes equations can be neglected.
g. The mud layer can be divided into several horizontal layers. For each layer, the viscosity is constant and equations of motion and continuity equation for Newtonian can be applied.
h. The whole part of the mud layer is in motion.
i. The viscosity of each layer takes the value corresponding to the mean motion of it.

(1) Governing Equations

We divide the fluid system into n layers as indicated in Fig. 2. The water layer is represented by $n=1$. Waves propagate in the x direction, and $\hat{u}_i$, $\hat{w}_i$ and $\hat{p}_i$ are the horizontal and vertical velocity and pressure within the i-th layer, respectively. Moreover, ρ_i, ν_i, and h'_i are the density, kinematic viscosity, and thickness of i-th layer, respectively. From the assumption f, the Navier-Stokes equations neglecting the convective accelerations can be represented as

$$\frac{\partial \hat{u}_i}{\partial t}=-\frac{1}{\rho_i}\frac{\partial \hat{p}_i}{\partial x}+\nu_i\left(\frac{\partial^2 \hat{u}_i}{\partial x^2}+\frac{\partial^2 \hat{u}_i}{\partial z^2}\right), \tag{7}$$

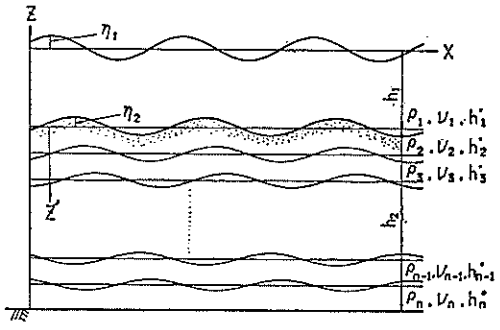

Fig. 2 Multi-Layered Model

$$\frac{\partial \hat{w}_i}{\partial t}=-\frac{1}{\rho_i}\frac{\partial \hat{p}_i}{\partial z}+\nu_i\left(\frac{\partial^2 \hat{w}_i}{\partial x^2}+\frac{\partial^2 \hat{w}_i}{\partial z^2}\right). \tag{8}$$

The continuity equation is

$$\frac{\partial \hat{u}_i}{\partial x}+\frac{\partial \hat{w}_i}{\partial z}=0. \tag{9}$$

By making use of Eq. (6), the kinematic viscosity ν_i in Eqs. (7) and (8) can be approximated as

$$\nu_i=\left(\mu_B+\frac{\tau_y}{\sqrt{4|\Pi_{ei}|}}\right)/\rho_i, \tag{10}$$

and using Eq. (4), $4|\Pi_{ei}|$ can be written as

$$4|\Pi_{ei}|=2\left(\frac{\partial \hat{u}_i}{\partial x}\right)^2+2\left(\frac{\partial \hat{w}_i}{\partial z}\right)^2+\left(\frac{\partial \hat{u}_i}{\partial z}+\frac{\partial \hat{w}_i}{\partial x}\right)^2. \tag{11}$$

We assume that the solutions $\hat{u}_i$, $\hat{w}_i$, and $\hat{p}_i$ are expressed in the following form:

$$\left.\begin{aligned}\hat{u}_i&=u_i(z)e^{i(kx-\sigma t)}\\ \hat{w}_i&=w_i(z)e^{i(kx-\sigma t)}\\ \hat{p}_i&=P_i(z)e^{i(kx-\sigma t)}\end{aligned}\right\}, \tag{12}$$

where, k is the wave number and σ the angular frequency.

Displacements of the water surface and interface are represented as the following relation

$$\eta_i=a_i e^{i(kx-\sigma t)}, \tag{13}$$

where the water surface is expressed as η_1 and the interface waves between the i-th and $(i+1)$-th layer is expressed as η_{i+1}. The wave number k is a complex number, namely,

$$k=k_r+ik_i. \tag{14}$$

Substituting Eq. (14) into Eq. (13), we can obtain the expression for the water surface and interfacial displacements as

$$\eta_i=a_i e^{-k_i x}e^{i(k_r x-\sigma t)}. \tag{15}$$

Therefore, the damping coefficient of wave heights is equal to k_i and the wave length is expressed as $L=2\pi/k_r$.

If the velocities and pressure $\hat{u}_i$, $\hat{w}_i$, $\hat{p}_i$ are represented by Eq. (12), the solutions of Eqs. (7)~(9) can be obtained as

$$\begin{aligned}w_i(z)=&A_i\sinh k\left(\sum_{j=1}^{i}h'_j+z\right)+B_i\cosh k\left(\sum_{j=1}^{i}h'_j+z\right)\\&+C_i\exp\left\{\lambda_i\left(\sum_{j=1}^{i}h'_j-h'_i+z\right)\right\}+D_i\exp\left\{-\lambda_i\left(\sum_{j=1}^{i}h'_j+z\right)\right\},\end{aligned} \tag{16}$$

$$u_i(z)=iw_i'/k, \tag{17}$$

$$P_i(z)=(\rho_i\nu_i/k^2)(w_i'''-w_i'\lambda_i^2), \tag{18}$$

$$\lambda_i^2=k^2-i\sigma\nu_i^{-1}, \tag{19}$$

where the prime for u_i and w_i represents the derivative of z. The complex constants A_i, B_i, C_i, D_i and the unknown variables k and a_i can be determined from the boundary conditions.

(2) Boundary Conditions

i) At the water surface ($z=\eta_1$)

The linearized kinematic condition and continuity of stress can be written as

$$\frac{\partial\eta_1}{\partial t}=\hat{w}_i, \tag{20}$$

$$\hat{p}_1-2\rho_1\nu_1\frac{\partial\hat{w}_1}{\partial z}=0, \tag{21}$$

$$\rho_1\nu_1\left(\frac{\partial\hat{u}_1}{\partial z}+\frac{\partial\hat{w}_1}{\partial x}\right)=0. \tag{22}$$

Taking Taylor's expansion of Eqs. (20), (21), and (22), we can get the following equations, namely,

$$-i\sigma a_1=A_1\sinh kh'_1+B_1\cosh kh'_1+C_1+D_1e^{-\lambda_1h'_1}, \tag{23}$$

$$M_1(A_1\cosh kh'_1+B_1\sinh kh'_1-2\rho_1\nu_1\lambda_i(C_1-D_1e^{-\lambda_1h'_1})-\rho_1ga_1=0,$$

$$M_1=i\rho_1\sigma/k-2\rho_1\nu_1k, \tag{24}$$

$$2A_1k^2\sinh kh'_1+2B_1k^2\cosh kh'_1+(\lambda_1^2+k^2)(C_1+D_1e^{-\lambda_1h'_1})=0. \tag{25}$$

ii) At the interface ($z=-\sum_{j=1}^{i}h'_j$)

The kinematic, continuity of velocity and stress conditions at the interface are

$$\frac{\partial\eta_{i+1}}{\partial t}=\hat{w}_i, \tag{26}$$

$$\hat{u}_i=\hat{u}_{i+1}, \tag{27}$$

$$\hat{w}_i=\hat{w}_{i+1}, \tag{28}$$

$$\hat{p}_i-2\rho_i\nu_i\frac{\partial\hat{w}_i}{\partial z}-\rho_ig\eta_{i+1}=\hat{p}_{i+1}-2\rho_{i+1}\nu_{i+1}\frac{\partial\hat{w}_{i+1}}{\partial z}-\rho_{i+1}g\eta_{i+1}, \tag{29}$$

$$\rho_i\nu_i\left(\frac{\partial\hat{u}_i}{\partial z}+\frac{\partial\hat{w}_i}{\partial x}\right)=\rho_{i+1}\nu_{i+1}\left(\frac{\partial\hat{u}_{i+1}}{\partial z}+\frac{\partial\hat{w}_{i+1}}{\partial x}\right). \tag{30}$$

From these equations we can get the following relations

$$-i\sigma a_{i+1}=B_i+C_ie^{-\lambda_ih'_i}+D_i, \tag{31}$$

$$B_i+C_ie^{-\lambda_ih'_i}+D_i=A_{i+1}\sinh kh'_{i+1}+B_{i+1}\cosh kh'_{i+1}+C_{i+1}+D_{i+1}e^{-\lambda_{i+1}h'_{i+1}}, \tag{32}$$

$$A_ik+C_i\lambda_ie^{-\lambda_ih'_i}-\lambda_iD_i$$
$$=A_{i+1}k\cosh kh'_{i+1}+B_{i+1}k\sinh kh'_{i+1}+C_{i+1}\lambda_{i+1}-D_{i+1}\lambda_{i+1}e^{-\lambda_{i+1}h'_{i+1}}, \tag{33}$$

$$M_iA_i-2\rho_i\nu_i\lambda_i(C_ie^{-\lambda_ih'_i}-D_i)$$
$$=M_{i+1}(A_{i+1}\cosh kh'_{i+1}+B_{i+1}\sinh kh'_{i+1})-2\rho_{i+1}\nu_{i+1}\lambda_{i+1}$$

$$\times(C_{i+1}-D_{i+1}e^{-\lambda_{i+1}h'_{i+1}})-(\rho_{i+1}-\rho_i)ga_{i+1},$$

$$M_i=\frac{i\rho_i\sigma}{k}-2\rho_i\nu_i k, \tag{34}$$

$$\rho_i\nu_i\{2B_ik^2+(\lambda_i^2+k^2)(C_ie^{-\lambda_ih'_i}+D_i)\}$$
$$=\rho_{i+1}\nu_{i+1}\{2A_{i+1}k^2\sinh kh'_{i+1}+2B_{i+1}k^2\cosh kh'_{i+1}$$
$$+(k^2+\lambda_{i+1}^2)(C_{i+1}+D_{i+1}e^{-\lambda_{i+1}h'_{i+1}})\}. \tag{35}$$

iii) At the rigid bottom $\left(z=-\sum_{j=1}^{n}h'_j\right)$

From the following equations

$$\hat{u}_n=0, \tag{36}$$

$$\hat{w}_n=0, \tag{37}$$

the boundary conditions at the rigid bottom can be represented as

$$kA_n+C_n\lambda_ne^{-\lambda_nh'_n}-\lambda_nD_n=0, \tag{38}$$

$$B_n+C_ne^{-\lambda_nh'_n}+D_n=0. \tag{39}$$

The unknown constants A_i, B_i, C_i, D_i, k, and a_2 to a_n are determined from these boundary conditions at the water surface, the interface and the rigid bottom. The kinematic viscosity ν_i still remains as an unknown constant and must be determined. The procedure in determining it is referred to in the next item.

(3) Equivalent Viscosity

In the case of a non-Newtonian fluid, the viscosity varies in space and time according to the variation of the deformation-rate. A rotary visco-meter has been used to obtain the relationship between the shear stress and shear strain. Under the action of surface waves, velocities and pressure vary with time making it difficult to estimate the viscosity reasonably in the wave field. As an approximation, *Gomei et al.*[12] have adopted a representative viscosity which is the minimum one corresponding to the measurable minimum shear strain. However, this method is not sufficient to treat the motion of a mud layer under the action of surface waves and so we seek an alternative method to reasonably estimate the viscosity in a wave field.

Damping of surface wave amplitudes on the basis of the interaction between the surface waves and a mud bed is mainly governed by energy dissipation within the mud bed. The rate of energy dissipation per unit volume is

$$\Phi=p^i{}_je^i{}_j. \tag{40}$$

From Eqs. (1), (3), (6), Φ can be represented for a Newtonian, power-law, and a Bingham fluid as

$$\Phi_N=4\mu_N|\Pi_e|, \tag{41}$$

$$\Phi_P=4K(4|\Pi_e|)^{(n-1)/2}|\Pi_e|, \tag{42}$$

$$\left.\begin{aligned}\Phi_B&=4\left(\mu_B+\frac{\tau_y}{\sqrt{4|\Pi_e|}}\right)|\Pi_e|,\ \left(\frac{1}{2}p^i{}_jp^j{}_i>\tau_y{}^2\right)\\&=0,\ \left(\frac{1}{2}p^i{}_jp^j{}_i\leqq\tau_y{}^2\right)\end{aligned}\right\} \tag{43}$$

respectively. Although the viscosity of a non-Newtonian fluid varies in space and time, we assume that a representative viscosity $\bar{\mu}_e$ exists which is the averaged value of an instantaneous one and it is a measure of the viscosity in a wave field. This gives an averaged energy dissipation function as

$$\bar{\Phi}=4\bar{\mu}_e\overline{|\Pi_e|}. \tag{44}$$

The term $\overline{|\Pi_e|}$ can be approximated by a Newtonian velocity field which is estimated by using the viscosity $\bar{\mu}_e$. The same relationship can be applied to a non-Newtonian fluid. Thus, the equivalent viscosities $\bar{\mu}_e$ for power-law and Bingham fluids can be expressed as

$$\bar{\mu}_e=K(\overline{4|\Pi_e|})^{(n-1)/2}, \tag{45}$$

$$\bar{\mu}_e=\mu_B+\frac{\tau_y}{\sqrt{\overline{4|\Pi_e|}}}, \tag{46}$$

respectively. In the case of a Bingham fluid, part of a mud layer does not deform if the shear stress is less than the yield stress. We, however, assume that whole part of the mud layer is in motion. We divide it into several horizontal layers, and it is assumed that within each layer either Eqs. (45) or (46) can hold.

An averaged objective $\overline{|\Pi_{ei}|}$ of the i-th layer can be calculated as follows. The real parts of Eq. (12) can be written as

$$\hat{u}_i(z)=|u_i|e^{-k_i x}\cos(k_r x-\sigma t+\alpha_i), \tag{47}$$

$$\hat{w}_i(z)=|w_i|e^{-k_i x}\cos(k_r x-\sigma t+\beta_i). \tag{48}$$

If we take the partial derivatives of Eqs. (47) and (48) with respect to x and z, the following relations can be obtained as

$$\frac{\partial\hat{u}_i}{\partial x}=-|k||u_i|e^{-k_i x}\sin(k_r x-\sigma t+\alpha_i+\theta_k), \tag{49}$$

$$\frac{\partial\hat{u}_i}{\partial z}=|u_i'|e^{-k_i x}\cos(k_r x-\sigma t+\alpha_i'), \tag{50}$$

$$\frac{\partial\hat{w}_i}{\partial x}=-|k||w_i|e^{-k_i x}\sin(k_r x-\sigma t+\beta_i+\theta_k), \tag{51}$$

$$\frac{\partial\hat{w}_i}{\partial z}=|w_i'|e^{-k_i x}\cos(k_r x-\sigma t+\beta_i'), \tag{52}$$

where α_i, β_i, α_i', β_i', and θ_k are the arguments of u_i, w_i, u_i', w_i', and k, respectively. The substitution of Eqs. (49)~(52) in Eqs. (11) leads to

$$\begin{aligned}4\overline{|\Pi_{ei}|}=\frac{1}{2}\{&|k|^2(2|u_i|^2+|w_i|^2)+(|u_i'|^2+2|w_i'|^2)\\&-2|u_i'||w_i||k|\sin(\beta_i+\theta_k-\alpha_i')\}e^{-2k_i x}.\end{aligned} \tag{53}$$

As can be expected from the above equation, $\overline{|\Pi_{ei}|}$ is a function of x and decreases with a rate twice larger than the surface wave damping Therefore, the equivalent viscosity $\bar{\mu}_e$ is also a function of x. In the following calculation, however, the equivalent viscosity is assumed to be constant in the x-direction and it is represented by the initial value where $x=0$. The reason is that the solution cannot

be obtained if the viscosity vary with the distance x. In this case, an approximate method can be adopted in which the total distance of calculation is divided into short sections within which the viscosity can be regarded as constant.

The procedure to obtain the equivalent viscosity is as follows: the velocity field corresponding to the initial value $\bar{\mu}_{e0}$ is calculated and from the velocity field, $\bar{\mu}_e$ is obtained by Eq. (45) or (46). An iteration procedure is repeated until the viscosity converges.

(4) Damping of the Surface Wave Amplitude by Viscous Dissipation near Side Walls

In the case of an experimental flume, viscous damping of the surface wave amplitude near the wall cannot be neglected because the viscosity of the mud $10^3 \sim 10^5$ times as large as water even in the case when water content is about 200%.

Based on the boundary layer approximation, *Hunt*[13] has obtained the damping of the surface wave amplitude by an energy dissipation within a laminar boundary layer. Using a method similar to the method of *Hunt*, we estimate the energy dissipation by calculating the velocity near the wall.

If we denote the rotational horizontal velocity within a side wall boundary layer in the i-th layer as $U_i(z)$, the equation of motion can be written as

$$\frac{\partial U_i}{\partial t}=\nu_i\frac{\partial^2 U_i}{\partial y^2}, \tag{54}$$

where y is directed from the center of the flume to the direction perpendicular to the x–z plane. At the center of the flume ($y=0$) U_i vanishes. The solution satisfying the boundary condition that $U_i=-\hat{u}_i$ at $y=-B/2$ (B is the width of the flume) is, then,

$$U_i(z)=-u_i(z)\exp\left\{-(1+i)\sqrt{\frac{\sigma}{2\nu_i}}\left(y+\frac{B}{2}\right)\right\}\exp\{i(kx-\sigma t)\}. \tag{55}$$

In the same manner stated above, the rotational vertical velocity $W_i(z)$ can be written as

$$W_i(z)=-w_i(z)\exp\left\{-(1+i)\sqrt{\frac{\sigma}{2\nu_i}}\left(y+\frac{B}{2}\right)\right\}\exp\{i(kx-\sigma t)\}. \tag{56}$$

The energy dissipation $-dE_i/dt$ which is averaged over a period of waves can be expressed as

$$-\frac{dE_i}{dt}=\frac{\rho_i\nu_i}{B}\int_{z_l}^{z_u}2\int_{-B/2}^{0}\left\{\overline{\left(\frac{\partial U_i}{\partial y}\right)^2}+\overline{\left(\frac{\partial W_i}{\partial y}\right)^2}\right\}dydz, \tag{57}$$

where $z_u=-\sum_{j=1}^{i}h'_j+h'_i$ and $z_l=-\sum_{j=1}^{i}h'_j$.

The real part of $\partial U_i/\partial y$ is expressed as

$$\frac{\partial U_i}{\partial y}=\sqrt{\frac{\sigma}{\nu_i}}|u_i|e^{-2k_i x}\exp\left\{-\sqrt{\frac{\sigma}{2\nu_i}}\left(y+\frac{B}{2}\right)\right\}$$
$$\times\cos\left\{k_r x-\sigma t-\sqrt{\frac{\sigma}{2\nu_i}}\left(y+\frac{B}{2}\right)+\frac{\pi}{4}\right\}. \tag{58}$$

From Eq. (58) we can obtain the following relation as

$$\overline{\left(\frac{\partial U_i}{\partial y}\right)^2}=\frac{\sigma}{2\nu_i}|u_i|^2e^{-2k_ix}\exp\left\{-\sqrt{\frac{2\sigma}{\nu_i}}\left(y+\frac{B}{2}\right)\right\}. \tag{59}$$

In the same way as Eq. (59) we can obtain the following relation as

$$\overline{\left(\frac{\partial W_i}{\partial y}\right)^2}=\frac{\sigma}{2\nu_i}|w_i|^2e^{-2k_ix}\exp\left\{-\sqrt{\frac{2\sigma}{\nu_i}}\left(y+\frac{B}{2}\right)\right\}, \tag{60}$$

for the component W_i.

The energy dissipation dE_i/dt is, then, given by

$$-\frac{dE_i}{dt}=\frac{\rho_i}{B}\sqrt{\frac{\sigma\nu_i}{2}}e^{-2k_ix}\left\{1-\exp\left(-\sqrt{\frac{B}{2\nu_i}}\right)\right\}\times\int_{z_l}^{z_u}(|u_i|^2+|w_i|^2)dz. \tag{61}$$

Moreover, the energy E averaged over a wave period is

$$\begin{aligned}\bar{E}&=\sum_{i=1}^{n-1}\overline{\left(2\int_{z_l+\eta_{i+1}}^{z_u+\eta_i}\rho_igzdz\right)}+\overline{2\int_{-(h_1+h_2)}^{-(h_1+h_2)+h'_n+\eta_n}\rho_ngzdz}\\&=\rho_1g\overline{\eta_1^2}+(\rho_2-\rho_1)g\overline{\eta_2^2}+\cdots.\\&\quad+(\rho_n-\rho_{n-1})g\overline{\eta_n^2}.\end{aligned} \tag{62}$$

For mud with a high water content, its density is 1.2~1.4 g/cm^3 and the wave heights within the mud are limited to 30~50% of the surface wave heights. Moreover, the second term and the following ones in the right-hand side of Eq. (62) are small compared with the first term provided that the density of mud does not vary abruptly. The enrgy $\bar{E}$ is then approximated by the following expression

$$\bar{E}\fallingdotseq\rho_1g\overline{\eta_1^2}=\frac{1}{2}\rho_1ga_1^2. \tag{63}$$

The total energy dissipation $d\bar{E}/dt$ over the whole mud layer is the sum of each layer dE_i/dt. If we make use of a group velocity C_g, we can obtain the rate of energy dissipation in space as

$$\frac{d\bar{E}}{dt}=\sum_{i=1}^{n}\frac{dE_i}{dt}=C_g\frac{d\bar{E}}{dx}. \tag{64}$$

Moreover, $d\bar{E}/dx$ can be written as

$$\frac{d\bar{E}}{dx}=\rho_1ga_1\frac{da_1}{dx}=-\rho_1ga_1^2k_{iw}, \tag{65}$$

where k_{iw} is viscous dissipation rate of wave amplitude. Integration of Eq. (65) leads to the following relation

$$a_1(x)=a_1(0)\exp(-k_{iw}x). \tag{66}$$

The damping coefficient k_{iw} can, then, be written as

$$k_{iw}=\sum_{i=1}^{n}\frac{dE_i}{dt}\Big/(\rho_1ga_1^2C_g). \tag{67}$$

Differentiation of the boundary conditions Eqs. (23)~(25), (31)~(35), (38), and (39) with respect to k leads to the simultaneous equations. The group velocity $C_g(=d\sigma/dk)$ can be estimated as the solution of these equations. The total damping coefficient is denoted as k_{it} which is the sum of k_i and k_{iw}. In the comparison of

wave damping between the experimental wave damping and the theory, the total damping coefficient k_{it} will be used.

(5) Movement of Fluid Particles

The horizontal and vertical displacements of a fluid particle from the mean position (x, z) can be calculated from Eqs. (47) and (48) as

$$\xi_i = -\frac{|u_i|}{\sigma} e^{-k_i x} \sin(kx - \sigma t + \alpha_i), \tag{68}$$

$$\zeta_i = -\frac{|w_i|}{\sigma} e^{-k_i x} \sin(kx - \sigma t + \beta_i). \tag{69}$$

(6) Procedure of Calculation

A flow chart for calculating the damping coefficient of the wave amplitude and the viscosity of the mud is shown in Fig. 3. For the water layer, the density, viscosity, and depth of water must be given. For the mud layer, the vertical distribution of density or water content, specific gravity of mud particle, the relationship between the water content and yield stress, and the depth of the mud layer must be given. For the surface waves, the wave height and period must be given. Based on the preliminary calculation, the mud bed is divided into three horizontal layers in the calculation in the present report.

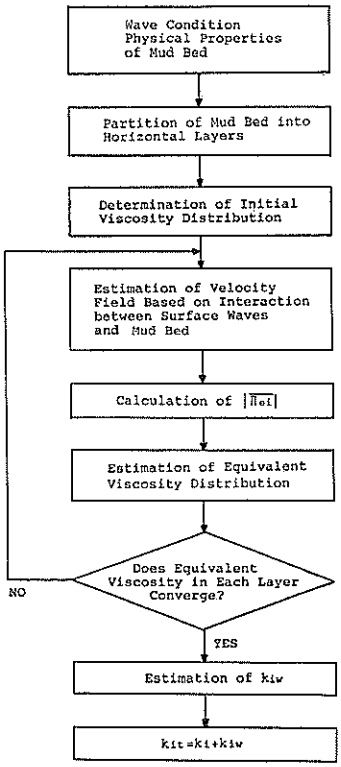

Fig. 3 Flow Chart in Calculating Wave Damping Coefficient

At first, the viscosities of the whole layers are assumed to be constant and the velocity fields calculated. Then, k, a_i, A_i, B_i, $\overline{C}_i$, and D_i are estimated by the boundary conditions. By using the calculated results of the velocity fields, $4|\overline{\Pi_{ei}}|$ is calculated and the corresponding equivalent viscosity is calculated for each layer. Again, $\bar{\eta}_{ei}$ is given as the viscosity of the i-th layer and the unknowns such as k are estimated by the boundary conditions. The procedures are repeated until the equivalent viscosity $\bar{\eta}_{ei}$ converges. From the solution of velocities, the group velocity C_g and the viscous damping coefficient k_{iw} near the walls are calculated. The total damping coefficient k_{it} is the sum of k_{iw} and k_i which is the solution of Eqs. (7)~(9).

Kaolinite clay and natural clay sampled at Kumamoto show the rheological properties as Bingham fluids. The relations between water content and the rheological properties of sample muds are obtained by the rotary visco-meter test and they are expressed as follows:

Kaolinite : $\tau_y=1.494\times10^{6}W^{-2.452}$(Pa),
$\mu_B=8.465\times10^{3}W^{-1.344}$(Pa·s),

Kumamoto mud : $\tau_y=1.008\times10^{14}W^{-5.796}$(Pa),
$\mu_B=1.295\times10^{4}W^{-1.436}$(Pa·s),

where, $W(\%)$ is water content. Relationships between the rate of deformation and shear stress for various values of water content are shown in Figs. 12 and 13 to appear later.

(7) Some Typical Properties of the Calculated Results

i) Effects of the number of divided layers

Figure 4 shows the relationship between the number of divided layers N (N= 1~10) and the damping coefficient k_i in the case of W=200%. The damping coefficient is almost constant when N is larger than 2. Figure 5 shows the vertical distribution of the equivalent viscosity. It gradually decreases with depth because the velocity gradient becomes greater near the bed.

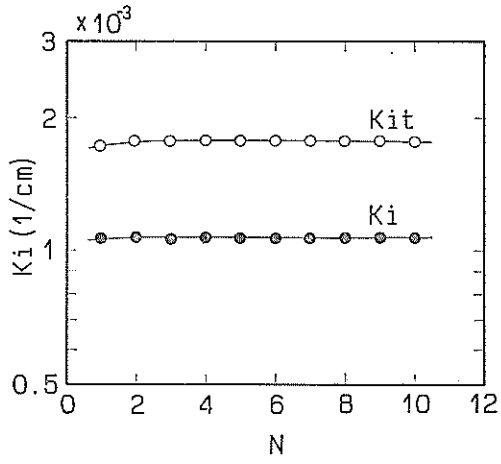

Fig. 4 Relationship between Number of Divided Layers N and Damping Coefficient k_i

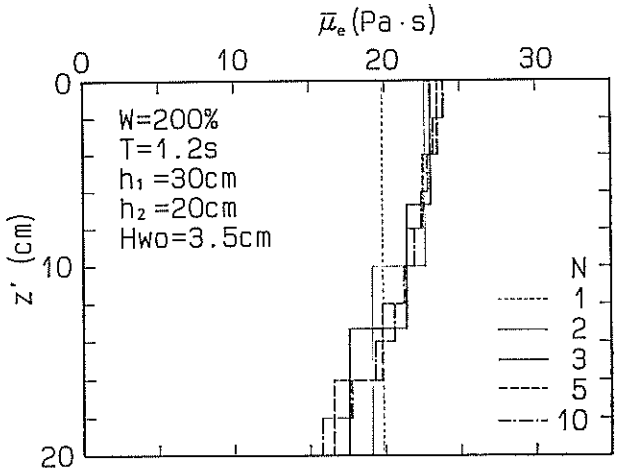

Fig. 5 Vertical Distribution of Equivalent Viscosity

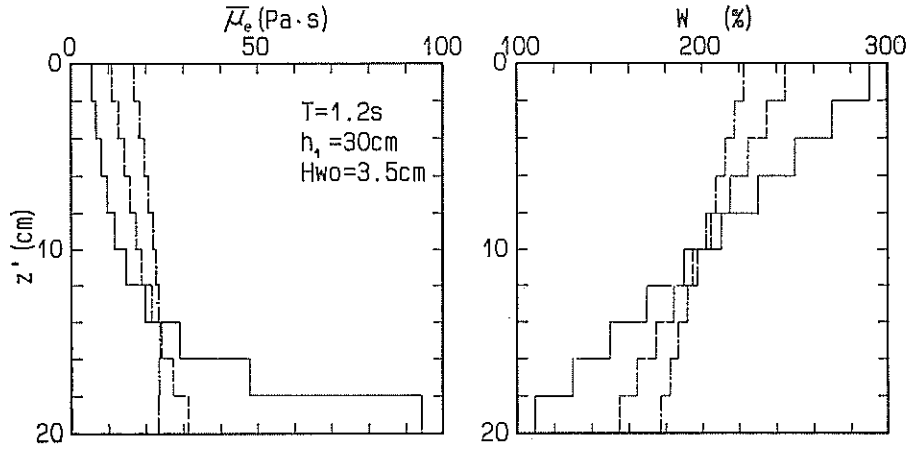

Fig. 6 Vertical Distributions of Equivalent Viscosity (left side) for Typical Water Content Distributions (right side)

For the distribution of water content as shown in the right hand side of Fig. 6, the distributions of the estimated equivalent viscosity are shown in the left hand side of Fig. 6. For three cases the mean values of water content ($W\%$) are the same. The vertical distribution of the equivalent viscosity varies according to the vertical distribution of W although the mean value of W is constant.

ii) Effects of the mud layer depth

Figure 7 shows the damping coefficients k_i and k_{it} and the wave length L. As the depth of mud layer becomes thick, the wave length L increases and so does the damping coefficient k_{it} which includes the viscous dissipation near the side walls. On

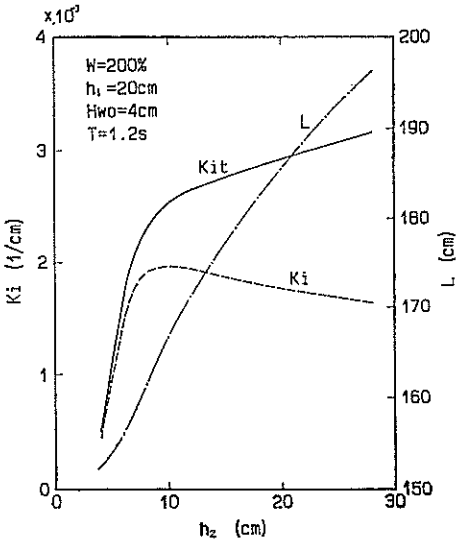

Fig. 7 Wave Damping Coefficient and Wave Length as a Function of Mud Layer Depth

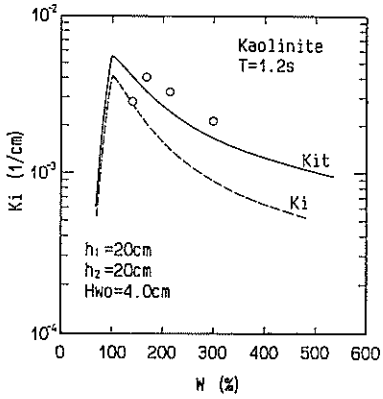

Fig. 8 Variation of Wave Damping Coefficient with Water Content

the other hand, in the case without effects of viscous damping near the side walls, the damping coefficient k_i has the maximum value when the depth of mud layer is nearly 10 cm.

iii) Effects of water content

Figure 8 shows the effect of water content (W) on the damping coefficient k_i and k_{it}. The damping coefficients increase as W decreases from 500%. They decrease, however, as W decreases from 100% because the equivalent viscosity increases abruptly. In the present method of calculation, the solution does not converge sufficiently for relatively large equivalent viscosity. The reason is that for a large equivalent viscosity, the calculated movement of the mud layer is very small and the equivalent viscosity becomes smaller for the next step in the iteration procedure. Finally, the equivalent viscosity becomes infinite and the motion of the mud layer converges to zero. This is the reason that the damping coefficients rapidly decrease for water contents of less than 100%. In this case, the iteration was automatically stopped after it was repeated eight times. The curves in this region, therefore, do not indicate the converged solutions.

iv) Effects of surface wave height

In the case of a Newtonian fluid, its viscosity is constant and the damping coefficient does not change for the theoretical calculation of *Dalrymple and Liu*[2]. In the case of a non-Newtonian fluid, however, the viscosity will vary with the surface wave height on account of the variation if the shear rate and the damping coefficient also vary with the wave height.

Figure 9 shows the relations between the wave height, the damping coefficient and the wave length. For wave heights larger than 1.5 cm, the damping coefficient decreases and the wave length increases as the wave height increases. For wave

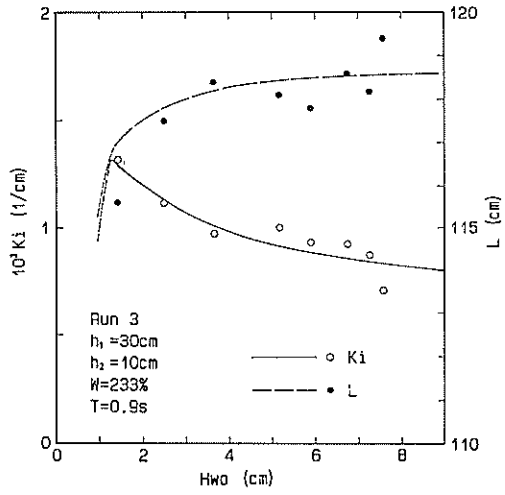

Fig. 9 Variation of Wave Damping Coefficient and Wave Length with Wave Height

heights less than 1.5 cm, a well converged solution cannot be obtained because the equivalent viscosity increases rapidly. The open and closed circles in Fig. 9 show the experimental data and are in satisfactory agreement with the theoretical curve.

2.3 Mass Transport Velocity

Nagai et al.[14] and *Shibayama et al.*[15] have measured the mass transport of a mud layer to the direction of the wave propagation. The typical transport processes of mud would be separated into three categories: namely, the first is that after the resuspension from the bed by waves it is carried away by currents, the second is that the bed material loosened by waves flows down along the slope and the third is the mass transport within a mud layer by wave action. The second and the third items are important even for small velocities because the densities of the moving layers are very high.

Here we calculate the mass transport velocity based on the theory of 2.2. The horizontal mass transport velocity U_{mi} and the vertical one W_{mi} can be written as

$$U_{mi}=\overline{\hat{u}_i}+\overline{\frac{d\hat{u}_i}{dx}\int_0^t \hat{u}_i dt}+\overline{\frac{d\hat{u}_i}{dz}\int_0^t \hat{w}_i dt}, \tag{70}$$

$$W_{mi}=\overline{\hat{w}_i}+\overline{\frac{d\hat{w}_i}{dx}\int_0^t \hat{u}_i dt}+\overline{\frac{d\hat{w}_i}{dz}\int_0^t \hat{w}_i dt}. \tag{71}$$

By making use of Eqs. (47)~(52) we can get the following relations

$$U_{mi}=\frac{1}{2\sigma}e^{-2k_i x}\{\cos\theta_k |k||u_i|^2-\sin(\beta_i-\alpha_i')|u_i'||w_i|\}, \tag{72}$$

$$W_{mi}=\frac{1}{\sigma}|k||u_i||w_i|e^{-2k_i x}\sin(\alpha_i-\beta_i)\sin\theta_k. \tag{73}$$

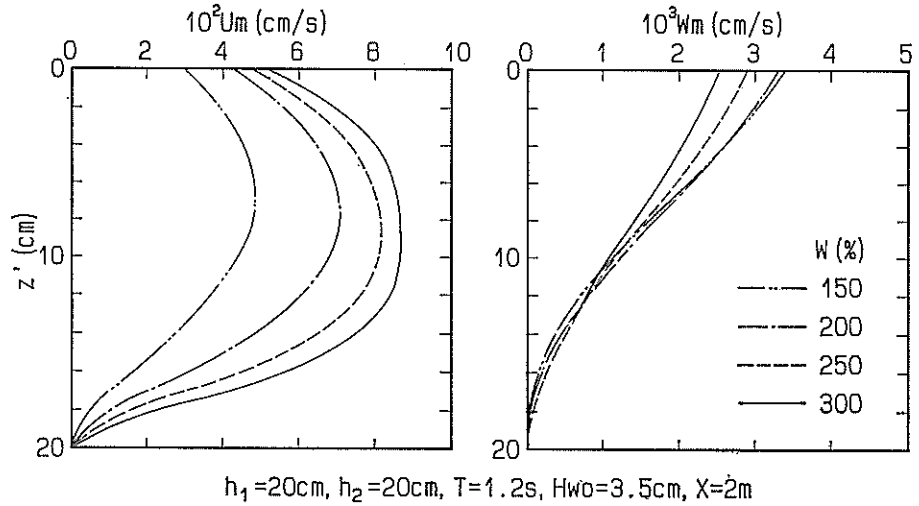

Fig. 10 Vertical Distribution of Calculated Mass Transport Velocity for Different Water Content

If there are no waves, $k_i=0$ and $\sin(\beta_i-\alpha_i')=-1$. Then U_{mi} becomes the same as the Stokes drift and $W_{mi}=0$.

Figure 10 shows examples of the theoretical distribution of mass transport velocities in the horizontal and vertical directions. The horizontal mass transport velocity U_m increases as the water content increases. The vertical mass transport velocity increases near the interface and it is expected that the water content increases as time passes. In Eqs. (72) and (73), the term $\exp(-2k_i x)$ is included so that the mass transport velocities decrease at a rate two times larger than the damping coefficient of the surface wave amplitude.

3. Experimental Equipment and Procedures

3.1 Experimental Equipment

The experiments were conducted in a wave-soil tank, which is shown in Fig. 11. The total length of the tank is 11 m. The dimensions of the test section are 400 cm long, 40 cm wide, and 50 cm deep. A movable floor is provided at the bottom of the test section and the level of the interface of mud layer and water can easily be adjusted to the level of the flume bottom. A plunger type wave maker is used to generate regular waves.

A settling tank with a depth of 2 m can be fitted above the test section of the flume to form a naturally settled mud bed (see Photo-1).

3.2 Experimental Procedures

(1) Physical Properties of Mud Used in the Experiment

Two types of mud materials were used in the experiment. One is mixture of kaolinite clay (Engel Hard, ASP600) and tap water, and the other is a natural clay sampled at Kumamoto Port. The physical properties of these samples are listed

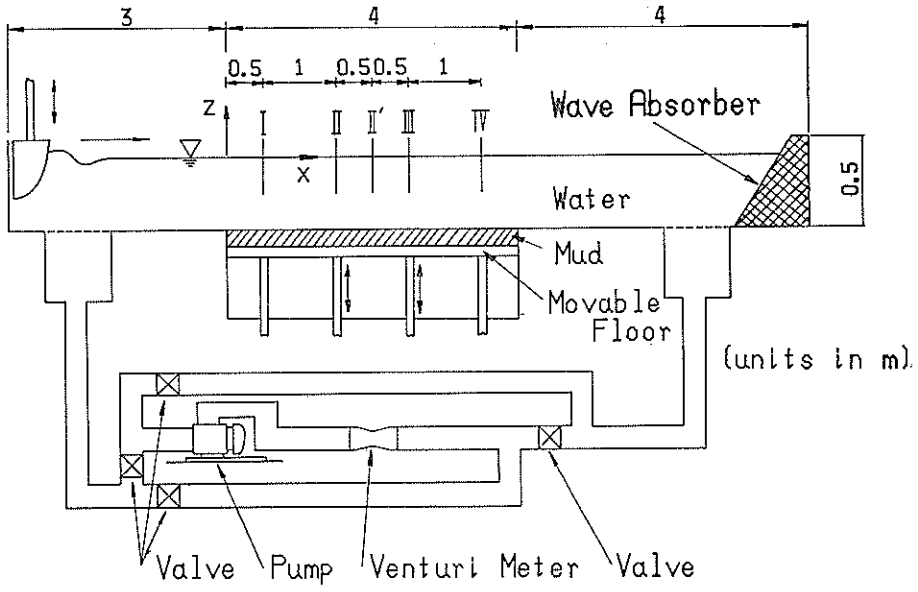

Fig. 11 Sketch of Wave-soil Tank

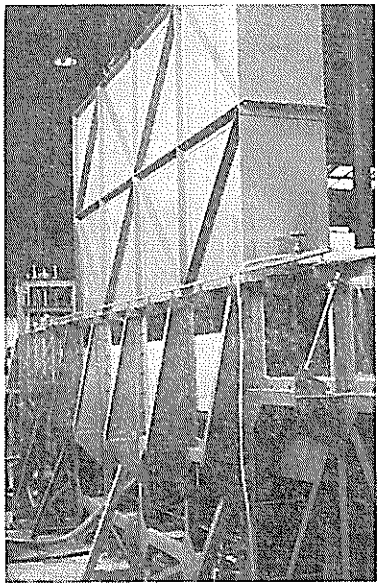

Photo 1 Wave-soil Tank and Settling Tank

Table 1 Physical Properties of Muds Used in the Present Experiment

Property \ Material	Kaolinite	Kumamoto Mud
Specific Gravity of Soil Particles	2.670	2.670
Liquid Limit (w_L)	70.5%	111.0%
Plastic Limit (w_p)	32.3%	41.9%
Plasticity Index (I_p)	38.2%	69.1%
Median Diameter (d_{50})	0.8μm	4.6μm
Ignition Loss	0%	9.1%

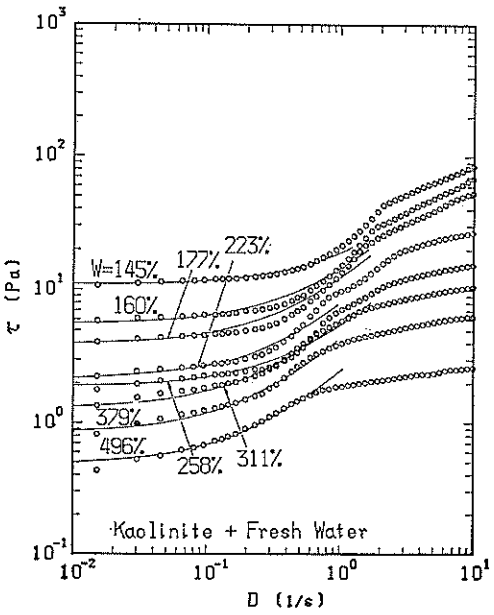

Fig. 12 Relationships between Rate of Deformation and Shear Stress for Kaolinite

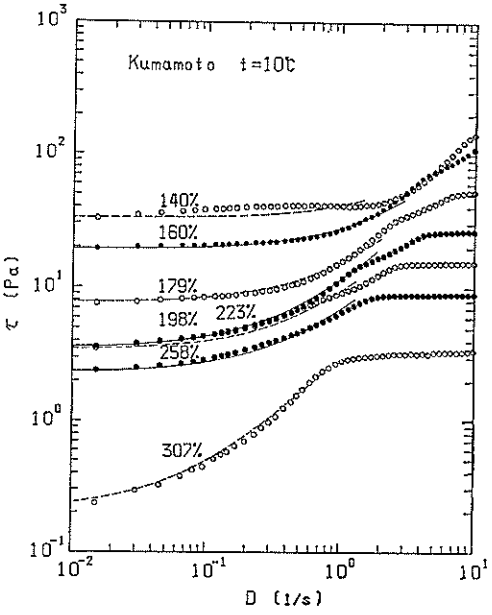

Fig. 13 Relationships between Rate of Deformation and Shear Stress for Kumamoto Mud

in Table 1.

Figure 12 shows the relationships between the rate of deformation and the shear stress of kaolinite for various levels of water content. Figure 13 also shows the similar relationships for Kumamoto mud. Tests were made by a Couette type viscometer which involves the laminar flow of a test fluid in annular space between two concentric cylinders (Contraves, Rheomat 115). The liquid used to adjust the water content is tap water for kaolinite and salt water (specific gravity is 1.03) for Kumamoto mud. The rate of deformation in the test was automatically controlled continuously by a personal computer from 0 to 10 s^{-1} (*Tsuruya et al.*[9]). The solid curves in the figure show the relationships of Bingham fluid, and can be expressed

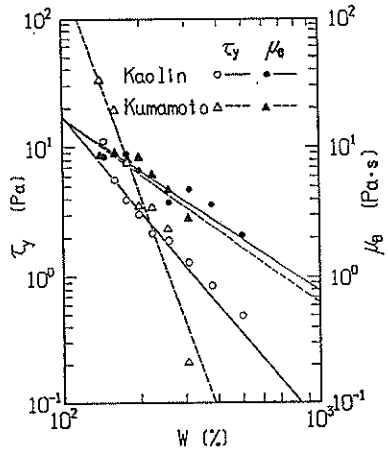

Fig. 14 Relationships between Yield Stress, Plastic Viscosity and Water Content

as

$$\tau=\tau_y+\mu_B D, \tag{74}$$

where τ_y is the yield stress and μ_B the plastic viscosity.

Application of Eq. (74) to the experimental data for a small value of the rate of deformation D leads to the yield stress τ_y and the plastic viscosity μ_B. Figure 14 shows the relationships between the water content W and τ_y, μ_B.

Applying the least square method to the data in Fig. 14, we can get the following relations for both materials:

Kaolinite : $\tau_y=1.494\times10^6 W^{-2.452}$(Pa)
$\mu_B=8.465\times10^3 W^{-1.344}$(Pa·s)
Kumamoto Mud : $\tau_y=1.008\times10^{14} W^{-5.796}$(Pa)
$\mu_B=1.295\times10^4 W^{-1.436}$(Pa·s)

The above relations have already been shown in 2.3(6).

(2) Bed Materials

a) Kaolinite Clay

Most of the experiments were performed with kaolinite clay which was a mixture of kaolinite and tap water. In order to make kaolinite clay, kaolinite powder was soaked in tap water for at least twenty-four hours. In the present experiment the water content of kaolinite was varied. For maintaining the good efficiency in the experiments, clay having the minimum water content was first used. Before the next experiment, the water content of the bed was changed by removing some of the clay and adding tap water of the same volume.

On the day of the experiment, the preparation of the mud bed was made in the morning and water was poured in the flume immediately. Experiments were conducted in the afternoon. Because the experiments were finished within several hours after the preparation of clay, it can be considered that the effects of consolidation were small. However, the mud with the water content larger than 300%

would be slightly affected by the consolidation.

b) Naturally Settled Mud

During stormy weather, bed materials are picked up by waves and mixed with sea water, and settle during calm weather. In this case, the water content within a mud layer decreases in the vertical downward direction on account of the consolidation. Thus, the behavior of the naturally settled mud would be different from that of thoroughly mixed mud.

In the present experiment, the mixture of kaolinite and tap water was poured into a settlement tank which was attached on the test section and a naturally settled mud bed was formed. The height of the settlement tank is 2 m and that of the wave-soil tank is 0.5 m. Accordingly, the maximum height of settlement is 2.5 m.

From the preliminary test, the final water content of the settled mud was deduced to be 220%. The total volume of the mixture to be poured was estimated so that the final depth of the settled mud would be 20 cm. The estimated heights and the initial water content of the mixture were 130 cm and 1570%.

Photos 2~4 show the situation of settlement at one day, two days, and ten days after the settlement, respectively. The interface is clearly identified in the photos. Figure 15 shows the time variation of the interface level measured in the tank. Because the side wall of the settlement tank are steel, the interface cannot be read

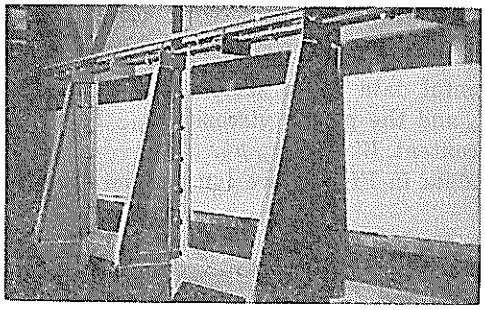

Photo 2 Settlement after one day

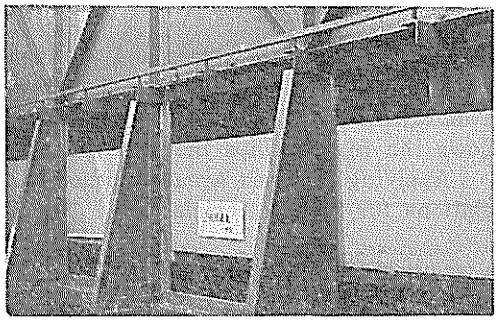

Photo 3 Settlement after two days

Photo 4 Settlement after ten days

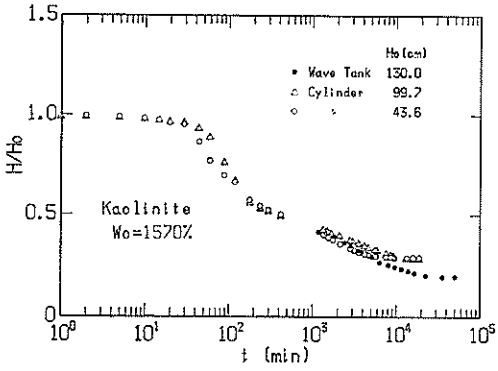

Fig. 15 Time Variation of Interface Level

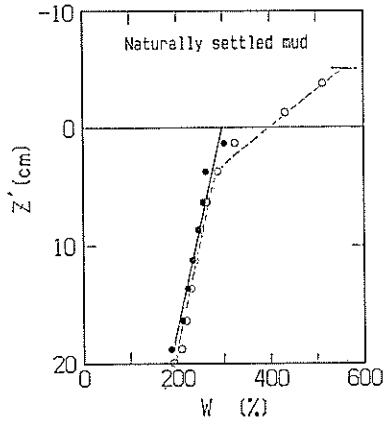

Fig. 16 Vertical Distribution of Water Content for Naturally Settled Mud

from the side during the early stages of the settlement. Therefore, settlement tests were conducted within acrylic cylinders which were filled with the sampled mixtures from the settlement tank. The lengths of the cylinders are 50 cm and 100 cm, 7 cm in diameter. The results are shown as open circles and triangles in the figure. The height of the interface (H) is divided by the initial depth (H_0). Up to 4000 minutes, the three types of data coincide each other. For longer times, however, settlements of the interface become small for acrylic cylinders and stop at nearly 10^4 minutes. For the tank, on the other hand, the settlement continues up to 2×10^4 minutes. This is because that the friction between the side wall and the mud layer is greater for acrylic cylinders than the settlement tank.

The same acrylic cylinder used in the settlement test was pushed in the mud layer and the undisturbed testing material was sampled. It was divided into many layers of a 2 cm deep and the water content of each layer was measured. Figure 16 shows the vertical distributions of the water content. The open circles show the water content 36 days after the beginning of the settlement. Near the interface, the water content is larger than 400% and rapidly decreases with depth. On the contrary, it gradually decreases below 6 cm from the interface. The depth of the settled mud layer was expected to be 20 cm. It was, however, 25.6 cm at the day of the test for the water content (36 days after the beginning of the settlement). The upper part of the mud layer was removed at the depth of 5.6 cm. Consequently, the depth of the naturally settled mud is 20 cm exactly (the same as the uniformly mixed mud layer. Solid circles show the vertical distribution of the water content after the elimination of the surface layer.

c) Kumamoto Mud

This mud was sampled at Ariake Bay in Kumamoto Pref. Its water content was nearly 140% and no preparations such as the mixing of sea water were made to avoid undesirable artificial effects as much as possible. The mud was relatively hard because of the low water content and because it was not uniform compared with kaolinite. Only for the Kumamoto mud, sea water drawn from Kurihama Bay

just in front of the authors' institute was used as the upper liquid. The specific gravity of the sea water used was 1.026.

(3) Types and Methods of Measurement

a) Wave Height

Measurements of wave heights were made at five stations I, II, II', III, and IV in Fig. 11. The locations of these stations from the beginning of the test section ($x=0$) were $x=0.5$, 1.5, 2.0, 2.5, and 3.5 m, respectively. From the measured wave heights, the damping coefficient k_i and the initial wave height H_{w0} were estimated. The wave length was estimated by the phase difference between the two wave gages.

b) Mud Wave Height

An ultra-sonic depth sounder was used to measure the movement of the interface. By using a signal conditioner and a DC amplifier, displacements of less than 1 mm could be measured accurately. Ultra-sonic waves with a frequency of 3 MHz was discharged from the probe so that continuous measurement of the interface was possible.

The arrangement of the sensors at Station III ($x=2.5$ m) is shown in Fig. 17. At the center of the flume, a wave gage, an ultra-sonic depth sounder, and two pore pressure transducers were installed at the locations, ①, ②, and ③, respectively.

c) Pore Pressure within Mud

Pore pressures within mud were measured with two pressure transducers as shown in Fig. 17. The depths of settlement are 2 cm and 5 cm from the interface.

d) Movement of Mud Particles

A method the same as that used by *Nagai et al.*[14] was employed to measure the movement of the mud particles. Acrylic rods 3 mm in diameter and 40 cm in length with a specific gravity of 1.36 were installed horizontally and perpendicular to the wave direction within the mud layer as markers. The movement of the tips of the rods were taken with a video camera through a glass wall. Horizontal and vertical amplitudes of the movements were read by a video position analyzer.

e) Velocity Distribution of Upper Layer

The two components electro-magnetic anemometer was used to measure the velocity of water. Measurements were made at the station II ($x=1.5$ m).

(4) Experimental Conditions

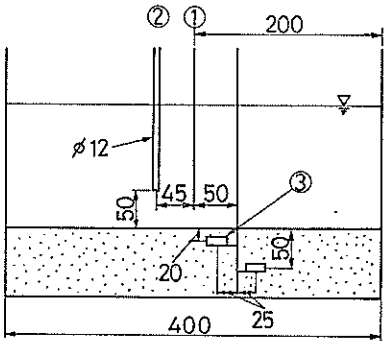

Fig. 17 Arrangement of Sensors

Table 2 Experimental Conditions

Case	Material	Water Content	Water Depth	Depth of Mud Bed	Wave Condition	
		$W(\%)$	h_1(cm)	h_2(cm)	T(s)	H_{wo}(cm)
A	Kaolinite	170~402	30	10	0.9	1~8
B	Kaolinite	168~228	20	10	0.7~1.4	3~5
C	Kaolinite	168~228	30	10	0.7~1.4	3~5
D	Kaolinite	142~300	20	20	0.7~1.4	3~5
E	Kaolinite	142~300	30	20	0.7~1.4	3~5
F	Naturally Settled Mud (Kaolinite)	246	20	20	0.7~1.4	3~5
G	〃	246	30	20	0.7~1.4	3~5
H	Kumamoto Mud	141	30	20	0.7~1.4	4, 6

Experimental conditions are listed in Table 2. Three types of mud (kaolinite, naturally settled kaolinite, and Kumamoto mud) were used as the bed material. The water depth of the upper layers was 20 cm and 30 cm. Another variables were the water content of the mud, the wave period, and the wave height.

4. Experimental Results and Discussion

4.1 Damping of Surface and Mud Waves

Figure 18 shows the longitudinal distributions of the surface and mud wave heights. The data is for kaolinite clay (W=227%). The solid and broken lines in the figure are drawn for the experimental data and show exponential decay to the direction of wave propagation. As expected from the theory, the damping coefficients of the surface and mud waves are nearly the same. The scatter of the data may have originated from the existence of reflected waves. The reflection coefficient is about 8% for the wave period T=0.8 s in the case of Fig. 18, and 14% for T=1.2 s. Figure 19 shows the same relations as Fig. 18 for Kumamoto mud. The scatter of the mud wave height is larger than that of the kaolinite clay. In the case of Kumamoto mud the water content is relatively low and viscous, so that it was not well mixed. Therefore, it can be considered that the viscosity, density and others are not so uniformly distributed as kaolinite. In fact, mud waves could be observed at some places but they could not be detected at some other places, though the distance between these places was only several centimeters. This is the reason why the damping coefficients of surface and mud waves differ themselves in Fig. 19.

Figure 20 shows the damping coefficient of surface wave heights as a function of the initial wave height H_{wo} (at x=0). The water content is chosen as a parameter. The curves in the figure are the theoretical ones. For small initial wave heights, the equivalent viscosity becomes so large that the solution does not converge; broken lines in this region represent the results of eight times iteration. Experimental results do not agree with the theory except for Run 3 and the experimental data of damping coefficient especially for high water content becomes large as the wave height becomes large. This result is contrary to that of 2.2(7). The wave height is varied from small to large one about seven or eight times in one run. As it took

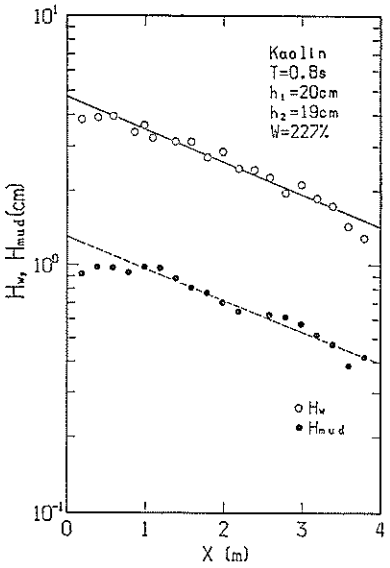

Fig. 18 Damping of Surface and Mud Waves (Kaolinite)

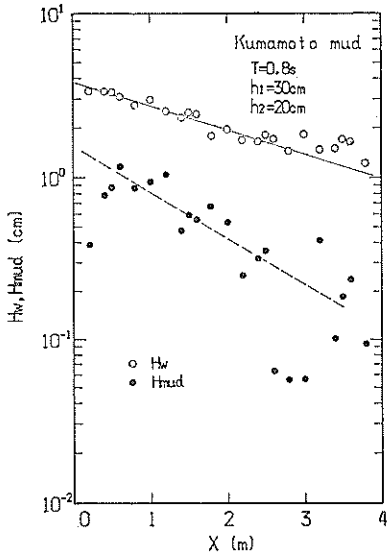

Fig. 19 Damping of Surface and Mud Waves (Kumamoto Mud)

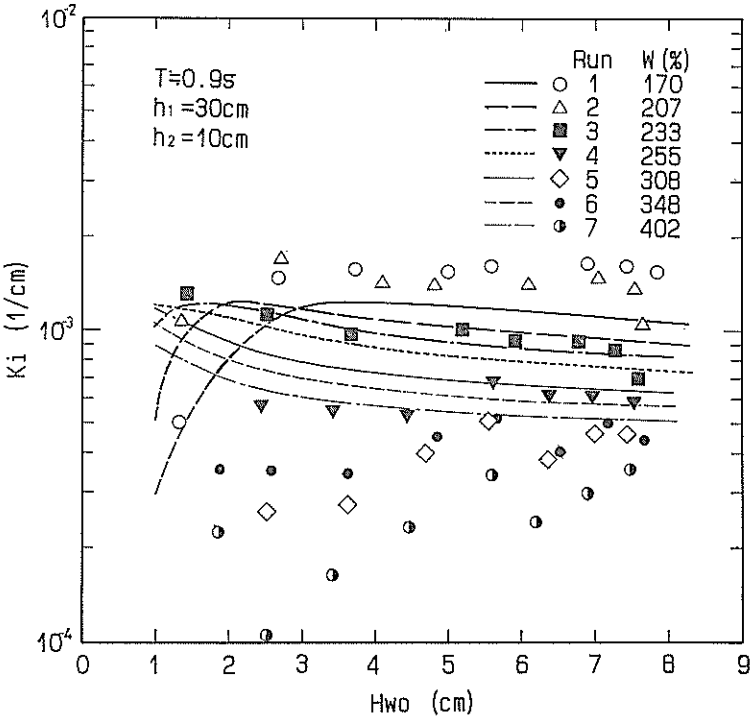

Fig. 20 Relationships between Wave Height and Damping Coefficient of Surface Waves (Case A)

about three hours for one run, the effect of consolidation might have influenced the result, especially for the run with high water content.

Figures 21~24 show the relationships between the wave period and the damping coefficient of wave height. Theoretical curves of k_{it} for various water content are also shown in the case of H_{w0}=4 cm (Case B, C) and H_{w0}=3.5 cm (Case D, E). In the case of Fig. 21 and 23 (water depth h_1 is 20 cm), experimental data agree with the theoretical curves. In the case of Fig. 23 (h_2=20 cm) experimental data for the case of W=142% are less than that of W=168%. It is suspected that the mud layer put into motion by surface waves could have been thinner for the cases of W=142% on account of high viscosity than for the case of 168% and thus the damping for the former was less than for the latter.

Figure 25 shows the same relation as Figs. 21~24 for the case of naturally settled mud. Numbers near the symbols show the wave heights. In this case, the damping coefficient k_i becomes large as the wave height becomes large. As the water content varies with depth, the effective mud depth due to wave action may also vary considerably. Therefore, theoretical calculations were made for both cases of h_2=20 cm and 10 cm. Measured damping factors for T=1.4 s show a rapid decrease but the theory does not explain this tendency.

For Kumamoto mud, the relationship between the damping coefficient and the wave period is shown in Fig. 26. This mud has the large yield stress τ_y. As the calculated viscosity near the interface becomes large, sufficient convergence of solutions cannot be obtained. From the observation of the experiment, it was observed that the mud layer within 2~3 cm from the interface was loosened on account of the wave motion and the water content of the surface mud layer became large with the passage of time. In such a case, it was confirmed that a well-converging solution

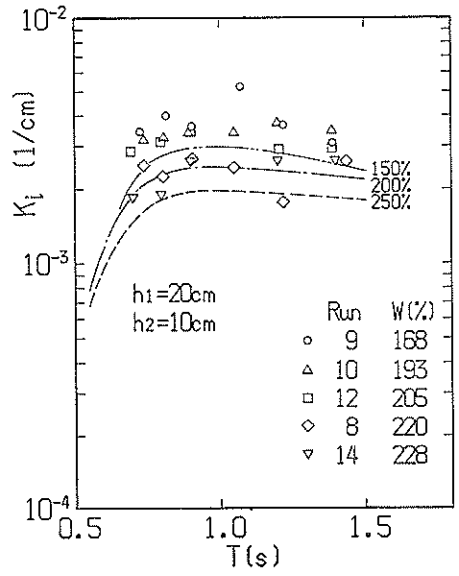

Fig. 21 Relationships between Wave Period and Damping Coefficient of Surface Waves (Case B)

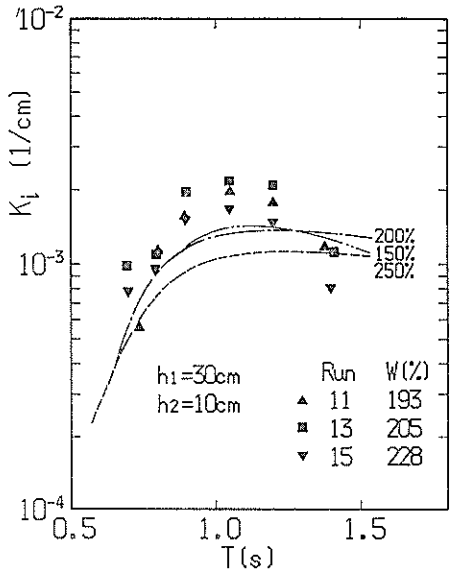

Fig. 22 Relationships between Wave Period and Damping Coefficient of Surface Waves (Case C)

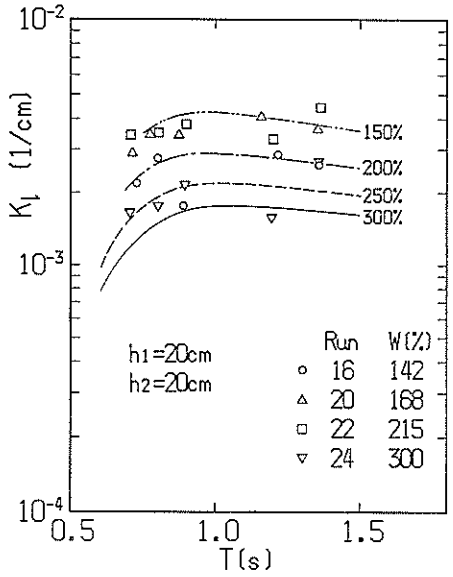

Fig. 23 Relationships between Wave Period and Damping Coefficient of Surface Waves (Case D)

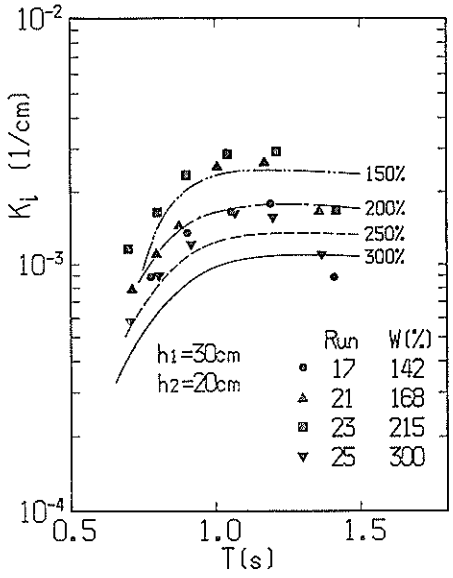

Fig. 24 Relationships between Wave Period and Damping Coefficient of Surface Waves (Case E)

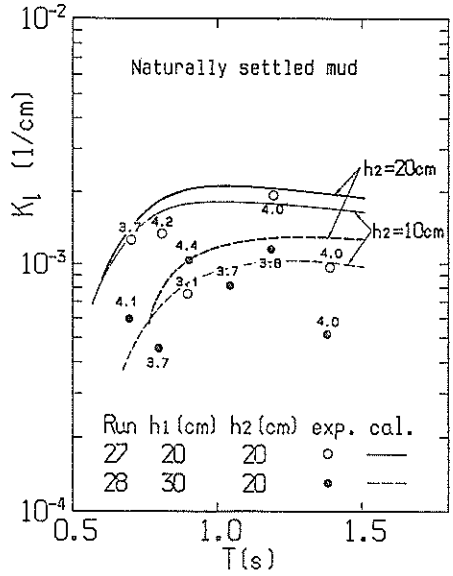

Fig. 25 Relationships between Wave Period and Damping Coefficient of Surface Waves (Naturally Settled Mud)

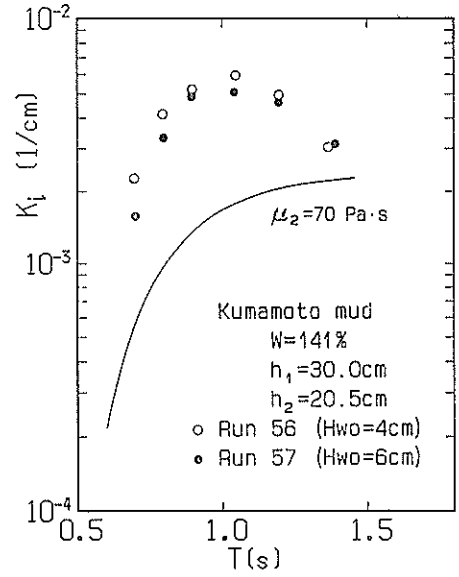

Fig. 26 Relationships between Wave Period and Damping Coefficient of Surface Waves (Kumamoto Mud)

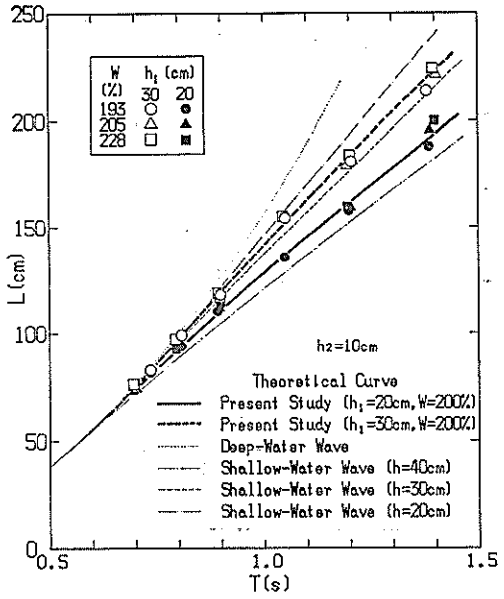

Fig. 27 Relationships between Wave Period and Length of Surface Waves (Case B, C)

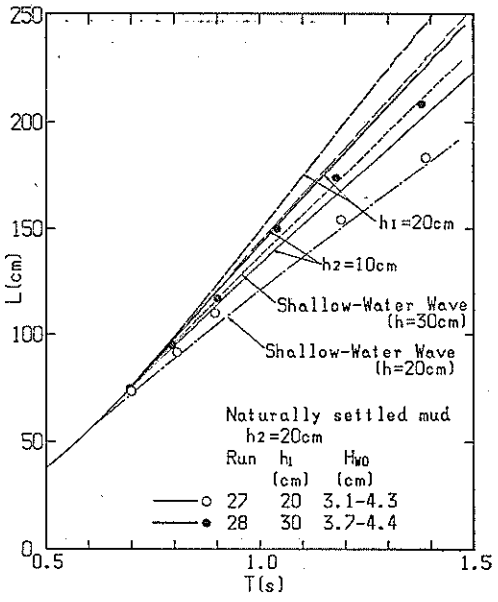

Fig. 28 Relationships between Wave Period and Length of Surface Waves (Naturally Settled Mud)

could be obtained if the water content was given as about 230% for the region from the interface to a level 2 cm below it. In the present experiment, however, the water content near the interface was not measured and so the theoretical relation shown in the figure only represents the result for the case that the water content is uniform and $\mu_2=70$ Pa·s which gives the maximum wave damping. As can be seen from the figure, the difference between the experimental data and the theory is large. In the case for low water content and high viscosity, therefore, the present model cannot accurately predict the magnitude of wave damping.

4.2 Wave Length

Relations between the wave length and period for the Case B and C ($h_2=10$ cm) are shown in Fig. 27. The wave length on a muddy bottom lies between that on the water depth h_1 and h_1+h_2 on the rigid bed. Figure 28 is for the case of the naturally settled mud. Theoretical calculation gives a larger wave length than the experiment if the depth of the mud layer is given as the actual depth of 20 cm ($h_2=$ 20 cm). The effective mud layer would be less than 20 cm, but even for the theoretical value of 10 cm mud depth ($h_2=10$ cm) there still remains some differences and the wave length is rather equal to that of a rigid bed.

4.3 Mud Wave Height

Figures 29 and 30 show the ratio of mud wave height to surface wave height. The depth of the mud layer (h_2) in Fig. 29 is 10 cm. The plotted data are those measured at the center of the tank. The experimental data are from 1.5 to 2 times larger than the theoretical value. This is because the mud wave height varies in

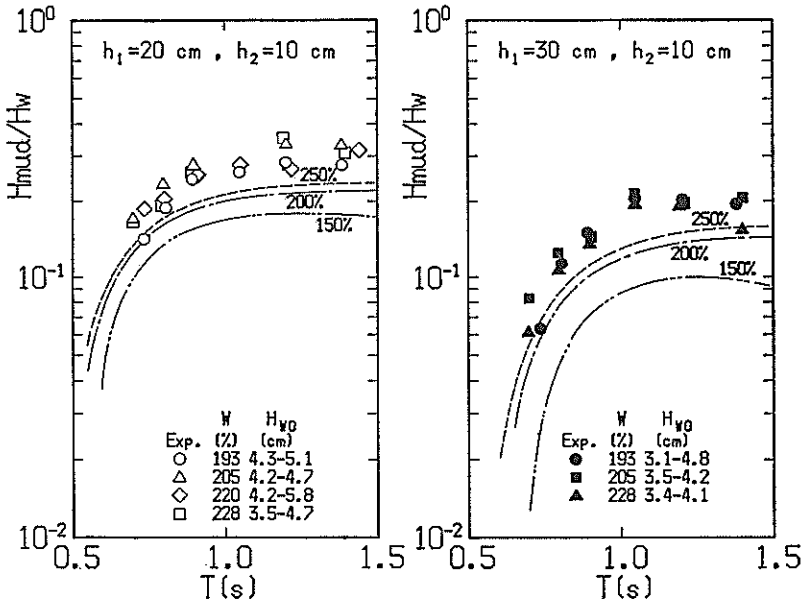

Fig. 29 Relationships between Wave Period and Ratio of Mud Wave Height to Surface Wave One (Case B, C)

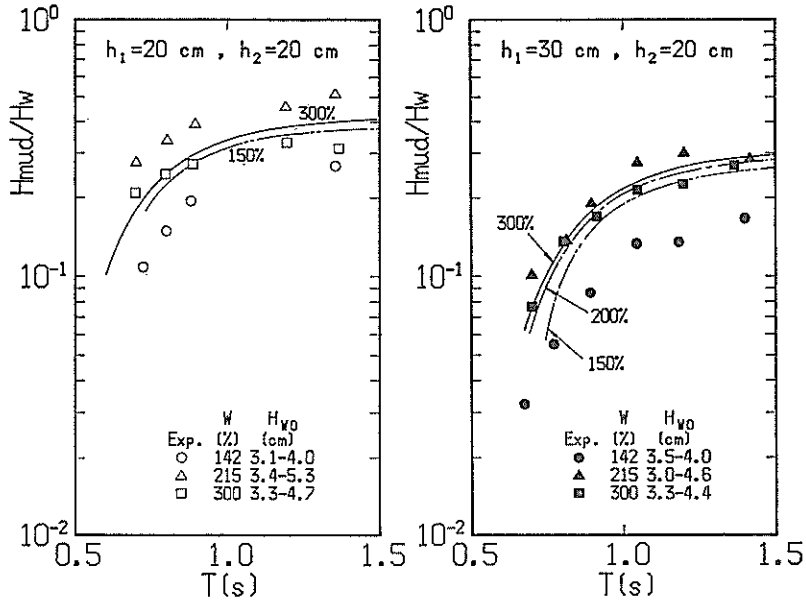

Fig. 30 Relationships between Wave Period and Ratio of Mud Wave Height to Surface Wave One (Case D, E)

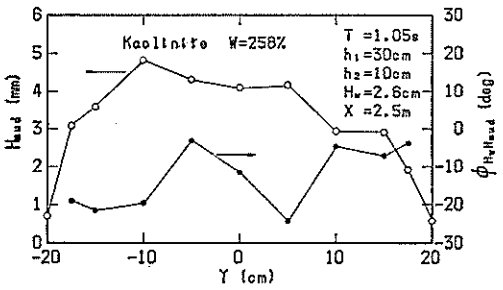

Fig. 31 Lateral Distribution of Mud Wave Height

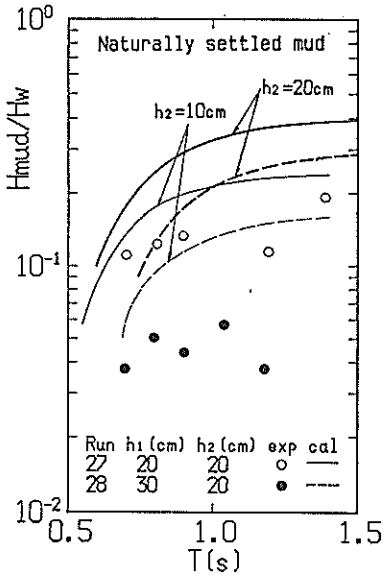

Fig. 32 Relationships between Wave Period and Ratio of Mud Wave Height to Surface Wave One

the lateral direction as shown in Fig. 31.

Figure 30 corresponds to the case with h_2=20 cm. Experimental data of H_{mud}/H_w for the case of W=142% are considerably small and is a consequence of high viscosity and small wave motion of the mud layer. Except for this case, the experimental data agree well with the theoretical curve compared with the case of Fig. 29.

The mud wave height varies in the lateral direction as shown in Fig. 31. Although the variation does not show the exact symmetry, it shows a rapid decrease near the wall and the maximum value near the center of the flume. The phase lag between surface and mud waves is also shown in the figure. The maximum phase lag is about 20°. Here we define the phase lag in such a way that a positive phase lag means the advance of the surface waves to mud waves. As the phase lag is negative in the figure, the mud waves are 5°~25° in advance of surface waves.

Figure 32 shows the same relationship as Figs. 29 and 30 for naturally settled mud. The theoretical relations for h_2=10 cm and 20 cm are also shown in the figure and these predict considerably greater mud wave heights than obtained by the experimental data. The reason is not clarified at this stage, but it can be attributed to the situation that in the present model it is difficult to give a reasonable effective depth of mud layer for a naturally settled mud.

4.4 Pressure within a Mud Layer

Figures 33 and 34 show the relative amplitude of pressure variation within a mud layer against the wave period. In the figure, the pore pressure is normalized with the hydrostatic pressure corresponding to the surface wave height. Figure 33 corresponds to the case of series B(h_2=10 cm). The theoretical curves are those

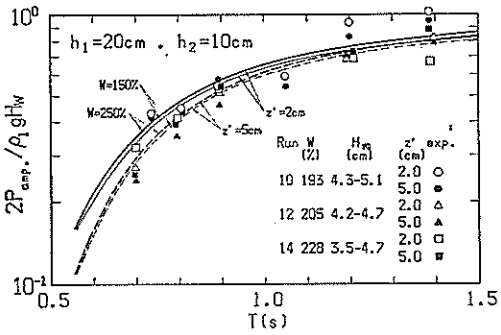

Fig. 33 Relationships between Wave Period and Amplitude of Pressure Within Mud Layer (Case B)

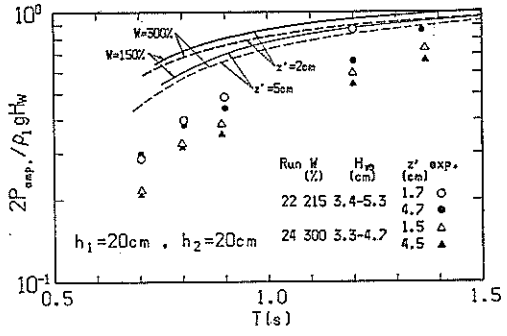

Fig. 34 Relationships between Wave Period and Amplitude of Pressure Within Mud Layer (Case D)

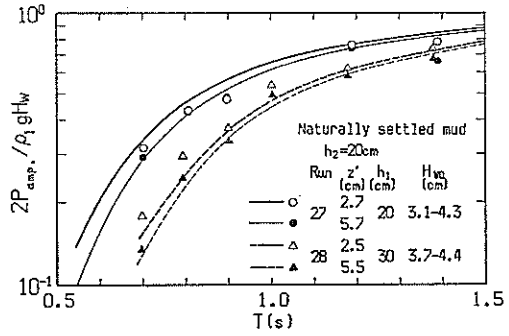

Fig. 35 Relationships between Wave Period and Amplitude of Pressure Within Mud Layer (Naturally Settled Mud)

for H_{w0}=4 cm and W=150% and 250%. Although the experimental data show some scattering, they are in agreement with the theoretical curves. Figure 34 corresponds to the case of h_2=20 cm. In contrast with Fig. 33 the theory gives a larger pressure than the experimental one. The difference between Figs. 32 and 33 implies that the downward propagation of pressure variation is smaller than the theoretical one in the case of h_2=20 cm. The experimental data in Fig. 34 are nearly equal to the theoretical curves in Fig. 33 for h_2=10 cm. From these facts, we may conclude that the movement of mud below 10 cm from the interface would be very small.

Figure 35 shows the relative amplitude of pressure variations within a mud layer against the wave period for the naturally settled mud. Experiments were conducted for h_2=20 cm, but the theoretical curves are drawn for the case of h_2= 10 cm. As in Fig. 34, the theoretical values would exceed the experimental data if the theoretical computations were made as h_2=20 cm. As we have described here, the theoretical curve agrees well with the experimental data when the theory is calculated for h_2=10 cm. As shown in Fig. 32, however, the experimental mud wave height is not consistent with the theoretical curve. Further theoretical development

is therefore necessary to clarify these points.

4.5 Mud Particle Motion

Figures 36 and 37 show the horizontal and vertical amplitudes of mud particle motions U_{xx} and U_{zz}, respectively. The theoretical relationships calculated from Eq.s (70) and (71) are also shown in the figures. Figure 36 corresponds to the case in which h_2=10 cm and the measuring position is x=2.5 m. Figure 37 corresponds to the case in which h_2=20 cm and x=1.5 m. In the theoretical calculation, the wave height is given as the measured wave height H_{w0} at x=0. Even in the case of kaolinite, the movement of the mud particles is not uniform and the measured data are scattered to some extent. However, the experimental data generally agrees well with the theoretical curves.

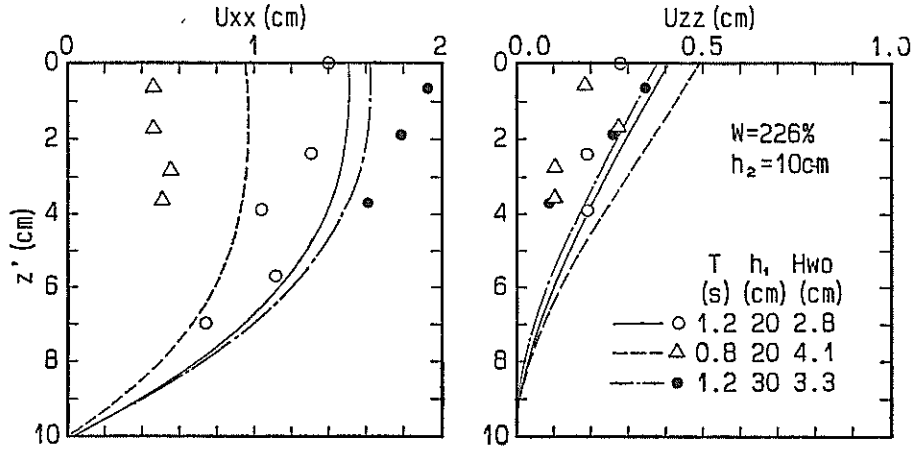

Fig. 36 Amplitude of Horizontal and Vertical Particle Motions (Case B, C)

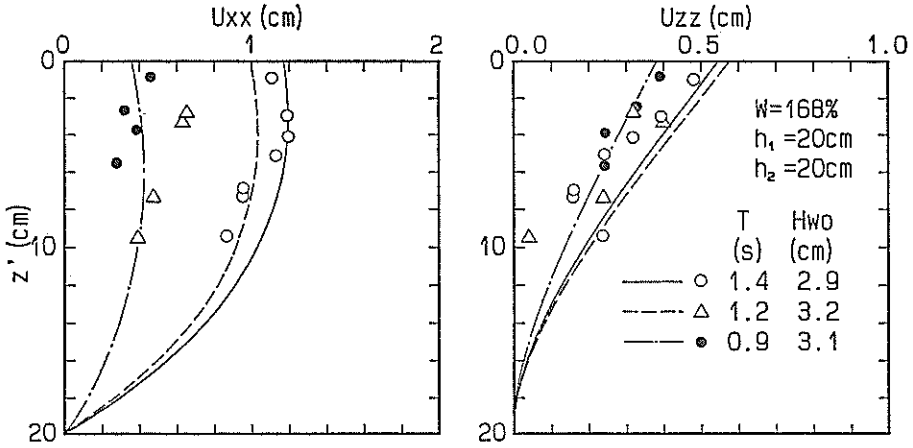

Fig. 37 Amplitude of Horizontal and Vertical Mud Particle Motions (Case D)

5. Conclusion

Theoretical and experimental study on the interaction between surface waves and a mud bed have been conducted. The following conclusion can be drawn from the present study:

1. The two-layered viscous fluid model by *Dalrymple and Liu* is extended to a multi-layered viscous fluid model. This model can take into account the vertical distribution of the mud characteristics (water content, mud density).
2. An equivalent viscosity is introduced to describe the flow field of a non-Newtonian fluid such as the Bingham or power law fluids.
3. It becomes possible to estimate a reasonable viscosity distribution within the mud layer with the assistance of the concept of the multi-layered viscous fluid model and the equivalent viscosity.
4. Equations to calculate the mass transport velocities in horizontal and vertical directions of mud layer are presented.
5. Three types of muds, namely, uniformly mixed kaolinite with tap water, naturally settled kaolinite, and Kumamoto mud were used to investigate the damping of surface and mud waves, pressure within the mud layer, and the amplitude of the particle motion of the mud.

Experimental data were compared with the proposed theoretical calculations and it became evident that the proposed multi-layered viscous fluid model using the equivalent viscosity can explain the experimental results for the most part. For Kumamoto mud, however, theoretical calculations do not necessarily explain the experimental data because the yield stress is relatively large.

(*Received on November 13, 1987*)

Acknowledgements

The authors wish to thank *Dr. Yoshimi Goda*, the Director General of the Port and Harbour Research Institute, for his critical review of the manuscript. The authors also wish to express their thanks to *Dr. Norio Tanaka*, formerly the Director of Marine Hydrodynamics Division at the same Institute, *Dr. Isao Irie*, the Director of Marine Hydrodynamics Division, and the members of the siltation research group of the Institute for their valuable discussion. Also, thanks are due to *Mr. Shuji Eguchi*, the member of Hydrodynamics Laboratory, for his assistance in typing the manuscript.

References

1) GADE, H. G.: Effects of a nonrigid, impermeable bottom on plane surface waves in shallow water, Jour. of Marine Research, Vol. 16, No. 2, pp. 61–82, 1958.
2) DALRYMPLE, A. R. and P. L. F. LIU: Waves over soft muds: a two-layer fluid model, Jour. of Physical Oceanography, Vol. 8, pp. 1121–1131, 1978.
3) HSIAO, S. V. and O. H. SHEMDIN: Interaction of ocean waves with a soft bottom, Jour. of Physical Oceanography, Vol. 10, pp. 605–610, 1980.
4) MACPHERSON, H.: The attenuation of water waves over a non-rigid bed, Jour. of Fluid Mech., Vol. 97, part 4, pp. 721–742, 1980.

5) YAMAMOTO, T., H. L. KONING, H. SELLMEIJER and E. V. HIJUM: On the response of a Polo-elastic bed to water waves, Jour. of Fluid Mech., Vol. 87, part 1, pp. 193–206, 1978.
6) YAMAMOTO, T., S. TAKAHASHI and B. SCHUCKMAN: Physical modeling of sea-sea-bed interactions, Jour. of Engineering Mech., ASCE, Vol. 109, No. 1, pp. 54–72, 1983.
7) YAMAMOTO, T. and B. SCHUCKMAN: Experiments and theory of wave-soil interactions, Jour of Engineering Mech., ASCE, Vol. 110, No. 1, pp. 95–112, 1984.
8) OTSUBO, K.: Experimental study on the physical and flow property of mud bed (*in Japanese*), Research Report from the National Institute for Environmental Studies, No. 42, pp. 1–177, 1982.
9) TSURUYA, H., S. NAKANO and J. TAKAHAMA: Investigation of Rheological Properties of Soft Muds with a Rotary Viscometer (*in Japanese*), Tech. Note of the Port and Harbour Res. Inst., No. 566, 29p., 1986.
10) FAAS, R. W.: Viscous Control of Estuarine Resuspension Patterns, Coastal Sediments '87, ASCE, Vol. 1, pp. 300–315, 1987.
11) TOMITA, Y.: Rheology —Mechanics of Non-Linear Fluids— (*in Japanese*), Corona, 444p., 1975.
12) GOMEI, M., E. YAUCHI, K. SAKAI, T. OTSUKI and N. ITOSU: Effects of muds on the interaction between surface waves and a mud bed (*in Japanese*), Proc. 33rd Japanese Conf. on Coast. Engng., pp. 322–326, 1986.
13) HUNT, J. N.: Viscous damping of waves over an inclined bed in a channel of finite width, La Houille Blanche, Vol. 7, pp. 836–842, 1952.
14) NAGAI, T., T. YAMAMOTO and L. FIGUEROA: Experiments on the interactive effects between surface waves and a soft mud bed (*in Japanese*), Proc. 30th Japanese Conf. on Coastal Engng., pp. 608–612, 1983.
15) SHIBAYAMA, T., H. TAKIKAWA and K. HORIKAWA: Mass transport of soft mud by surface waves (*in Japanese*), Proc. 32nd Japanese Conf. on Coastal Engng., pp. 258–262, 1985.